Novel carbon nanomaterials for the direct methanol fuel cell electrodes

Maryam Borghei

A'' Aalto University

Novel carbon nanomaterials for the direct methanol fuel cell electrodes

Maryam Borghei

A doctoral dissertation completed for the degree of Doctor of Science (Technology) to be defended, with the permission of the Aalto University School of Science, at a public examination held at the lecture hall TU1 of the school on 24 April 2015 at 12.

Aalto University
School of Science
Deprtment of Applied Physics
NanoMaterials Group

Supervising professor
Prof. Esko Kauppinen

Thesis advisor
Dr. Virginia Ruiz

Preliminary examiners
Prof. Magnus Rønning, NTNU, Norway
Dr. Frédéric Jaouen, Université Montpellier II, France

Opponent
Prof. Naotoshi Nakashima, Kyushu University, Japan

NORDIC ECOLABEL
441   697
Printed matter

Abstract

Direct methanol fuel cells (DMFC) are great candidates for portable power source applications. However, the sluggish reaction kinetics are key challenges in DMFC technology. The state-of-the-art electrocatalysts are Pt-based catalysts supported on carbon black. However, the high price of Pt, corrosion of carbon support and Pt degradation are the main problems.

In this thesis, carbon nanomaterials, namely few-walled carbon nanotubes (FWCNTs) and graphitized nanofibers (GNFs) were used as catalyst supports in the search for stable and durable catalysts. PtRu nanocatalysts with similar particle size and composition were synthesized and deposited on FWCNTs and GNFs. The electrochemical activities for methanol oxidation were compared with that of PtRu-carbon black in acidic conditions. The half-cell electrochemical measurements revealed higher activity with PtRu-GNFs and PtRu-FWCNTs. Later, the electrocatalysts were tested in macro- and micro-DMFC. The results revealed the significant influence of the catalyst support, inomer contect, electrode structure, preparation method, as well as the fuel cell architecture on the performance of a specific electrode material. The results also highlighted the necessity of electrode composition optimization when applying new materials at the electrodes, in order to achieve the best activity and durability for a certain electrocatalyst.

A special effort was also done to achieve Pt-free electrocatalysts with high activity for the oxygen reduction reaction (ORR) by introducing nitrogen heteroatoms in carbon nanomaterials, namely FWCNTs and graphite nanoplatelets (GNPs). N-FWCNTs exhibited remarkable electrocatalytic activity for ORR in alkaline media, despite their very low nitrogen content (~0.5 at.%). N-FWCNTs performed on par or better than a commercial Pt-C at the cathode of an alkaline DMFC. The N-GNPs exhibited enhanced electrocatalytic activity for ORR compared to pristine GNPs in alkaline media. The results indicated that N-doped carbon nanomaterials could be promising alternatives to their Pt counterparts to reduce fuel cell costs. However, further investigations are necessary to ascertain the real active sites in order to design more efficient and durable ORR electrocatalysts.

Preface

This research was carried out between Dec. 2009 and July 2014 in Nanomaterials Group (NMG) at the Department of Applied Physics, Aalto University School of Science. The Academy of Finland and the Research Foundation of Helsinki University of Technology are gratefully acknowledged for financial support of this work.

I would like to thank my supervisor, Prof. Esko I. Kauppinen for providing me with the opportunity to do my PhD in his laboratory and the support during my studies. I am also grateful to my instructor Dr. Virginia Ruiz for her guidance and pushing me forward with new ideas to undertake multidisciplinary work. I would like to convey special thanks to Dr. Tanja Kallio and her fuel cell group for being always helpful and encouraging. Their facilities and expertise have mad an important contribution to this thesis. I also would like to thank Dr. Petri Kanninen for his efforts carrying out the fuel cell tests and Dr. Annukka Santasalo-Aarnio for her expertise in electrochemical characterizations and our fruitful discussions.

I also would like to thank Dr. Gianmario Scotti for fabricating the micro fuel cells and his supervisor Prof. Sami Franssila. Thanks to Dr. Jani Sainio for always being welcome to receive my samples for XPS characterization, as well as Dr. Toma Susi for the fruitful discussions and guide in physical characterizations. I would like to acknowledge Dr. Divya Srivastava and Prof. Kari Laasonen for leading the project for the computational study of ORR on N-CNTs.

To all NMG colleagues, I would like to give my sincere gratitude for their help. I am also thankful to Prof. Albert Nasibulin and Dr. Ilya Anoshkin for providing me the FWCNTs and the useful comments. I also acknowledge Showa Denko Company for providing GNF material. Thanks to Dr. Hua Jiang for his help in TEM characterization. My warm hugs to Mrs. Marita Halme for always being a quick help with my official issues. I also thank my summer students, Meri Lundahl and Henri Tuominen for their hard work.

I am particularly grateful to Dr. Kaido Tammeveski for hosting me a visit in his laboratory in University of Tartu (Estonia) and sharing his expertise in electrochemistry. I greatly admire his personality, hospitality and the support during my visit and afterwards. I also thank Dr. Ivar Kruusenberg for his kind help in the lab and other students who welcomed me to work in their friendly atmosphere. They made such a useful and memorial visit for me.

My kind gratitude belongs to Dr. Shuang Ma Anderson and Prof. Eivind Skou, who kindly hosted me in their group in Southern University of Denmark and IRD fuel cell Company. I also thank Dr. Serban Stamatin for such nice work we built up together. I really enjoyed our collaboration and hope we can continue our productive work in future.

Furthermore, I would like to thank Dr. Janne Halme and Dr. Kerttu Aitola from New Energy Technologies Group in Aalto. I enjoyed our collaboration and discussions to develop Pt-free counter electrode for dye the solar cells. I also would like to give sincere thanks to Dr. Muhammad Imran Asghar and Dr. Syed Ghufran Hashmi for being such supportive and encouraging friends.

Moreover, I would like to thank Dr. Virgina Ruiz and her colleagues in IK$_4$-CIDETEC (Spain) for preparing a visit for me. I should specially remember Dr. Oscar Loaiza and Dr. Pedro Lamas for characterizing my catalysts for biosensing applications.

Finally, I would like to express my warm love and special gratitude to my parents who always supported me through my life. Big thanks to my brother for always being encouraging and supporting for my academic career. I am also thankful to my friends in Finland for being there for me in sadness and happiness. Especially, to Ms. Hoda Faghankhani and Shahpar Moradi whom are gifted to my life like lovely sisters.

Today is the "thanksgivings day". When I look back over every moments of my life, I have so many reasons to thank God for all the blessings given to me ☺

Espoo, Nov. 28th, 2014
Maryam Borghei

1

Contents

List of publications

This thesis consists of an overview of the following publications which are referred in the text by their Roman numerals.

I. A. Santasalo-Aarnio, M. Borghei, I.V. Anoshkin, A.G. Nasibulin, E.I. Kauppinen, V. Ruiz, T. Kallio; Durability of different carbon nanomaterial supports with PtRu catalyst in a direct methanol fuel cell, International Journal of Hydrogen Energy 37 (2012) 3415-24.

II. M. Borghei, G. Scotti, P. Kanninen, T. Wekman, I.V. Anoshkin, A.G. Nasibulin, S. Franssila, E.I. Kauppinen, T. Kallio, V. Ruiz; Enhanced performance of a silicon microfabricated direct methanol fuel cell with PtRu catalysts supported on few-walled carbon nanotubes, Energy 65 (2014) 612-20.

III. P. Kanninen, M. Borghei, V. Ruiz, E.I. Kauppinen, T. Kallio, The effect of Nafion content in a graphitized carbon nanofiber-based anode for the direct methanol fuel cell, International Journal of Hydrogen Energy 37 (2012) 19082-91.

IV. M. Borghei, P. Kanninen, M. Lundahl, T. Susi, J. Sainio, I.V. Anoshkin, A.G. Nasibulin, T. Kallio, K. Tammeveski, E.I. Kauppinen, V. Ruiz, High oxygen reduction of few-walled carbon nanotubes with low nitrogen content. Applied Catalysis B: Environmental 158-159 (2014) 233-41.

V. M. Borghei, I. Azcune, PM. Carrasco, J. Sainio, E.I. Kauppinen, V. Ruiz, Nitrogen-doped graphene with enhanced oxygen reduction activity produced by pyrolysis of graphene functionalized with imidazole derivatives. International Journal Hydrogen Energy 39 (2014) 24, 12749-56.

Author's contribution

I. The author synthesized all the catalyst materials and carried out physico-chemical characterizations. The results were interpreted and the manuscript prepared together with co-authors.

II. The research plan was defined together with the second author. The author prepared all the catalyst materials and performed the physico-chemical characterizations. The author interpreted the results together with co-authors and wrote the manuscript together with co-authors.

III. Catalyst material synthesis and physico-chemical characterizations were performed by the author. The manuscript was written together with co-authors.

IV. The author defined the research plan, synthesized the catalyst materials and carried out the physico-chemical and electrochemical characterizations. The author interpreted the results together with co-authors and wrote the manuscript.

V. The author prepared the catalyst materials, performed physico-chemical and electrochemical characterization of the catalysts. The author interpreted the results and wrote the manuscript together with co-authors.

Other publications not included in the thesis

1.   S.N. Stamatin, <u>M.Borghei</u>, R. Dhiman, S.M. Andersen, V. Ruiz, E.I. Kauppinen, E.M. Skou, Activity and stability of platinized multi-walled carbon nanotubes as fuel cell electrocatalysts, Applied Catalysis B: Environmental 162 (2015) 289.

2.   P. Kanninen, <u>M. Borghei</u>, Ruiz, V., Kauppinen, E.I., and Kallio, T., The effect of FAA3 content in a N-doped FWCNT-based cathode in anion exchange membrane fuel cell, Applied Catalysis B: Environmental 156-157 (2014) 341.

3.   D. Srivastava, T. Susi, <u>M. Borghei</u>, K. Laasonen, Dissociation of oxygen molecule on pristine and nitrogen doped carbon nanotubes: Spin-polarized density functional study, RSC Advances 4 (2014) 15225.

4.   S. Andersen, <u>M. Borghei</u>, H. Jiang, V. Ruiz, E. Kauppinen, E. Skou, Adsorption behavior of perfluorinated sulfonic acid ionomer on highly graphitized carbon nanofibers and their thermal stabilities, J. Phy. Chem.C 118 (2014) 10814.

5.   S. N. Stamatin, <u>M. Borghei</u>, S. Ma Andersen, S. Veltze, V. Ruiz, E. Kauppinen, E. M. Skou; Influence of different carbon nanostructures on the electrocatalytic activity and stability of Pt-supported electrocatalysts, Int. J of Hydrogen Energy 39 (2014) 8215.

6.   S. Andersen, <u>M. Borghei</u>, H. Jiang, V. Ruiz, E. Kauppinen, E. Skou, Interaction of multi-walled carbon nanotubes with perfluorinated sulfonic acid ionomers and surface treatment studies, Carbon 71 (2014) 218.

7.   P. M. Carrasco, S. Montes, I. Gracia, <u>M. Borghei</u>, H. Jiang, I. Odriozola, G. Cabanero, V. Ruiz, High-concentration aqueous dispersions of graphene produced by exfoliation of graphite using cellulose nanocrystals, Carbon 70 (2014) 157.

8.   P. J. Lamas-Ardisana, O.A. Loaiza, L. Anorga, E. Jubete, <u>M. Borghei</u>, V. Ruiz, E. Ochoteco, G. Cabanero, H. Grande, Disposable amperometric biosensor based on lactate oxidase immobilized on platinum nanoparticle-decorated carbon nanofibers and poly(diallyldimethylammonium chloride) films, Biosensors and Bioelectronics 56 (2014) 345.

9.   S. Ma Andersen, M. Borghei, P. Lund, E. Yli-Rantala, A. Pasanen, E.I. Kauppinen, V. Ruiz, P. Kauranen, E. Skou, Durability of carbon nanofiber (CNF) & carbon nanotube (CNT) as catalyst support for Proton Exchange Membrane Fuel Cells, Solid State Ionics 231 (2013) 94.

10.   K. Aitola, J. Halme, S. Feldt, P. Lohse, M. Borghei, A. Kaskela, A. Nasibulin, E. Kauppinen, P. Lund, G. Boschloo, A. Hagfeldt, Highly catalytic carbon nanotube counter electrode on plastic for dye solar cells utilizing cobalt-based redox mediator, Electrochimica Acta 111 (2013) 206.

11.   P. Kanninen, M. Borghei, Ruiz, V., Kauppinen, E.I., and Kallio, T., The effect of Nafion content in a graphitized carbon nanofiber-based anode for the direct methanol fuel cell, International Journal of Hydrogen Energy 37 (2012) 19082.

12.   K. Aitola, M. Borghei, A. Kaskela, E. Kemppainen, A. Nasibuline, E. Kauppinen, P. Lund, V. Ruiz, J. Halme, Flexible metal free counter electrode for dye solar cells based on conductive polymer and carbon nanotubes, Electroanalytical chemistry 13 683(2012) 70.

13.   E. Sairanen, M. Borghei, R. Karinen, Preparation methods for multiwalled carbon nanotubes supported palladium catalysis, Chemcatchem 4 (2012) 2055.

14.   N.Izadi, M. Borghei , A. Rashidi, R. Karimzadeh, A. Tofigh, Synthesis of carbon nanofibers over nanoporous Ni-MgO catalyst: Influence of the bimetallic Ni-(Cu, Co, Mo) MgO catalysts, J. of Experimental Nanoscience 7 (2012) 160.

15.   A. Santasalo, M. Borghei, IV. Anoshkin, Nasibulin, A. G., Kauppinen, E. I., Ruiz, V., Kallio T., Durability of different carbon nanomaterial supports with PtRu catalyst in a direct methanol fuel cell, Int. J. of Hydrogen Energy 37 (2011) 3415.

16.   E. Yli-Rantala, A. Pasanen, P. Kauranen, V. Ruiz, M. Borghei, E. Kauppinen, A. Oyarce, G. Lindbergh, C. Lagergren, M. Darab, S. Sunde, M. Thomassen, S. Ma-Andersen, E. Skou, Graphitised Carbon Nanofibers as Catalyst Support for PEMFC, Fuel Cells 11 (2011) 715.

17.   E. Rikkinen, A. Santasalo, S. Airaksinen, M. Borghei, V. Viitanen, J. Sainio, E. Kauppinen, T. Kallio, O. Krause, Atomic Layer Deposition Preparation of Pd Nanoparticles on a Porous Carbon Support for Alcohol Oxidation, J. Phy. Chem.C 115 (2011) 23067.

18.   M. Borghei, R. Karimzadeh, A. Rashidi, Nosrat Izadi, Kinetics of Methane Decomposition to COx-free Hydrogen and Carbon nanofiber over Ni-Cu/MgO Catalyst, Int. J. of Hydrogen Energy 35 (2010) 9479.

List of abbreviations and symbols

AEM	anion exchange membrane
AFC	alkaline fuel cell
BET	Brunauer-Emmett-Teller theory of adsorption
CB	carbon black
CL	catalyst layer
CNF	carbon nanofiber
CNT	carbon nanotube
CNM	carbon nanomaterial
DMFC	direct methanol fuel cell
DL	diffusion layer
DWCNT	double-walled carbon nanotube
EC	exchange capacity
EDXS	energy-dispersive X-ray spectroscopy
EIS	electrode impedance spectroscopy
FAA3	alkaline anion exchange membrane (FumaTech)
FWCNT	few-walled carbon nanotube
GNF	graphitized carbon nanofiber
GNP	graphene nanoplatelet
GNS	graphene nanosheets
GO	graphene oxide
IC	ionic capacity
IMFC	indirect methanol fuel cell
MEA	membrane-electrode assembly
MOR	methanol oxidation reaction
MWCNT	multi-walled carbon nanotube
Nafion®	sulphonated tetrafluorethylene copolymer (Du Pont)
NHE	normal hydrogen electrode
OCV	open circuit voltage
ORR	oxygen reduction reaction
PEFC	polymer electrolyte fuel cell
PEM	polymer electrolyte membrane
PTFE	polytetrafluoroethylene (Teflon ®)
RDE	rotating disk electrode
RE	reference electrode
RHE	reversible hydrogen electrode
RRDE	rotating ring disk electrode
SCE	Saturated calomel electrode
SEM	scanning electron microscopy
SWCNT	single-walled carbon nanotube
TEM	transmission electron microscopy
TGA	thermogravimetric analysis
WE	working electrode
XPS	X-ray photoelectron spectroscopy
XRD	X-ray diffraction
A	area (cm^2)
C	concentration
D	Diffusion coefficient
E	fuel cell voltage
F	Faraday's constant (96485.31 C mol^{-1})
j	current density (A cm^{-2})
n	number of electrons
υ	kinematic viscosity
ω	electron rotation rate (rad s^{-1})

1 Introduction

Increasing energy demand, depletion of fossil fuel reserves and the climate change related to the release of greenhouse gases has forced governments to invest on the new energies. Fuel cells are promising solutions for energy and environmental crisis due to their low emission and high efficiency (~80%). Polymer electrolyte fuel cells convert chemical energy of a fuel (hydrogen/alcohol) to electricity and provide wide range of applications in transportation, stationary and portable power supplies.

Fuel cell is composed of three active components: a fuel electrode (anode), an oxidant electrode (cathode) and an electrolyte between them. Five major types of fuel cells can be distinguished by the type of the electrolyte: Alkaline fuel cells (AFC), proton exchange membrane fuel cells (PEMFC), anion exchange membrane fuel cells (AEMFC), solid oxide fuel cells, phosphoric acid fuel cells and molten carbonate fuel cells [1].

The principle of a hydrogen fuel cell was first introduced in 1839 by Sir William Robert Grove, who tried to reverse the phenomenon of water splitting by applying electric field to hydrogen and oxygen. Fuel cell was first put to use in 1960s to provide electricity onboard the Gemini and Apollo spacecraft. During 1970s, fuel cell technology was developed for systems on earth. In 1980s, it began to be tested for the purpose of utilities and automobile sectors [2].

Fuel cells using methanol can be divided into two categories: indirect methanol fuel cell (IMFC) and direct methanol fuel cell (DMFC). DMFC technology was first developed in Jet Propulsion Laboratory in 1992. Methanol is an attractive fuel because it is cheap, easy to store and handle. In addition, there is no C-C bond to break and it has high volumetric energy density 4.3 kWh L^{-1}, i.e. almost twice that of liquid hydrogen (2.4 kWh L^{-1}). The fuel for portable applications should be of high volumetric energy density. DMFCs are potential due to high mass energy density, simple set-up and availability of liquid fuel, easy refilling. However, methanol involves some safety risks such as toxicity and flammability [3].

In a DMFC the main challenge is the sluggish methanol oxidation at the anode. However, oxygen reduction reaction (ORR) at the cathode is even six times slower. The state-of-the-art commercial catalysts are Pt (at cathode) and bimetallic PtRu (at anode) on a high area carbon support, commonly carbon black, together take more than 50% of fuel cell cost. Another problem relates to the aggregation of catalyst particles under fuel cell operating condition due to the carbon corrosion, Pt aggregation and Ru dissolution; consequently performance may decrease continuously over time. Therefore, worldwide commercialization of fuel cells still remains a challenge, due to the durability issues and CO poisoning of Pt catalysts [4] as well as the limited resources and high cost of platinum (~ $1200/ounce in Feb. 2015).

1.1 Scope of the thesis

The objective of this doctoral thesis is to enhance DMFC performance through synthesis of more efficient electrocatalysts. Our strategy is based on application of novel carbon nanomaterials (CNM) as carbon support for PtRu catalysts, and also using them as Pt-free electrocatalysts. Different types of CNMs have been used in this study such as carbon nanotubes (CNTs), carbon nanofibers (CNFs) and graphene. These novel carbon materials are very good candidates for catalysis application because of their high surface area, superior electrical conductivity and electron transfer properties as well as thermal and mechanical stability.

The goal of the thesis is approached in two ways; firstly few walled carbon nanotubes (FWCNTs) and graphitized nanofibers (GNFs) were used as alternative carbon support for PtRu to achieve more active and durable electrode for methanol oxidation at the PEM-DMFC anode. Secondly, FWCNTs and graphite nanoplatelets (GNPs) were modified by nitrogen doping in order to completely replace Pt catalyst, acting as Pt-free electrocatalysts for ORR at the cathode of an AEM-DMFC. Figure 1.1 illustrates the scope of the thesis. The red circle covers the study on using CNMs as catalyst support and investigation of performance at the anode of a PEM-DMFC (Publications I, II & III). The green circle encompasses the study on nitrogen doping of CNM as Pt-free electrocatalyst for ORR at the cathode of an AEM-DMFC (Publications IV & V).
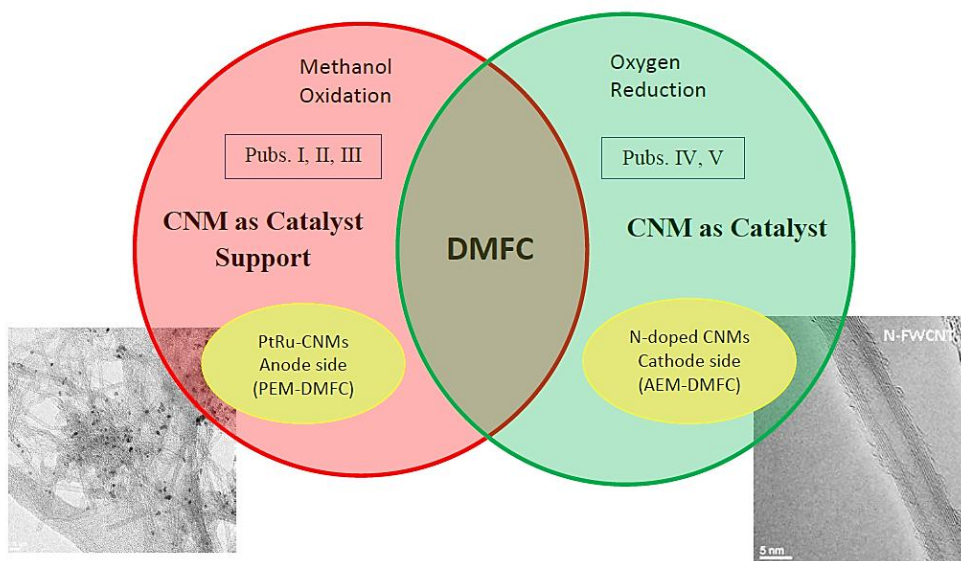
Figure 1.1. Scope of the thesis; red circle: PtRu-CNM for MOR at the anode in PEM-DMFC, green circle: N-CNM for ORR at the cathode in AEM-DMFC.

In Publication I, PtRu catalysts with similar particle size and composition were deposited on novel nanocarbon supports: FWCNTs, GNFs, and the traditional carbon black (Vulcan). The catalytic activity of catalysts for methanol oxidation reaction was investigated in an electrochemical cell. In addition, fuel cell performance was examined in a macro scale PEM-DMFC (7.29 cm^2) for 6-day

long measurement. PtRu-GNF worked as the most durable electrode, among the three electrocatalysts.

In Publication II, the PtRu-catalysts supported on CNMs were prepared and their performances were investigated at the anode of a silicon microfabricated PEM-DMFC (1 cm^2) for continuous 3-day measurements. PtRu-FWCNTs and PtRu-GNFs showed respectively 471% and 274% enhancement in power density compared to PtRu-Vulcan.

In Publication III, Nafion content in the membrane electrode assembly (MEA) for PtRu-GNFs electrocatalyst was varied (30-70 wt.%) for optimization of the electrode structure. MEA with 50 wt.% Nafion content showed the best activity and stability in constant current measurements for 9 days in the macro-size PEM-DMFC (7.29 cm^2).

In Publication IV, nitrogen-doped FWCNTs (N-FWCNTs) were synthesized via a post-treatment doping method by coating FWCNTs with polyaniline (PANI) and then pyrolysis at high temperatures. The effect of PANI amount, pyrolysis temperature and functionalization of FWCNTs on the type of nitrogen-functional groups and the ORR activity was investigated. The resulting N-FWCNTs showed much higher electrocatalytic activity for ORR in alkaline media, despite of very low nitrogen content (0.5 at. %). The performance was also studied at the cathode of an AEM-DMFC and exhibited similar performance to a commercial Pt-C catalyst.
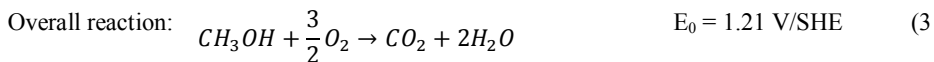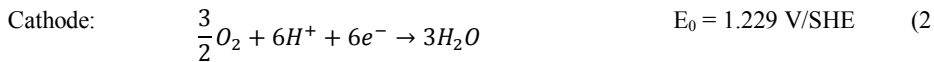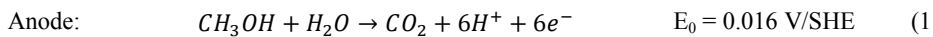
In Publication V, nitrogen doped-GNPs (N-GNPs) were prepared by thermal annealing of GNP functionalized with a series of imidazole-based nitrogen containing precursors of different nature, charge and nitrogen content. N-GNPs with 1.6-3.3 at.% nitrogen content showed enhanced electrocatalyst activity for ORR in alkaline media compared to the pristine GNP.

2 Background

2.1. Direct methanol fuel cell

The processes occurring in both PEM and AEM fuel cells are illustrated in Figure 2.1. In PEM-DMFC, methanol is fed to the anode where it is electrochemically oxidized to CO_2 and protons. Protons migrate though the membrane, and electrons are forced through an external circuit to the cathode. At the cathode, ORR occurs in which electrons and protons react electrochemically with oxygen molecules to produce water and heat.

The reactions at anode and cathode of PEM-DMFC are as below:

Anode: $$CH_3OH + H_2O \rightarrow CO_2 + 6H^+ + 6e^-$$ $E_0 = 0.016$ V/SHE   (1

Cathode: $$\frac{3}{2}O_2 + 6H^+ + 6e^- \rightarrow 3H_2O$$ $E_0 = 1.229$ V/SHE   (2

Overall reaction: $$CH_3OH + \frac{3}{2}O_2 \rightarrow CO_2 + 2H_2O$$ $E_0 = 1.21$ V/SHE   (3

The maximum theoretical voltage attainable from the overall reaction is 1.21 V with a theoretical efficiency of 96.5%, but in practice this voltage is not obtained due to poor electrode reaction kinetics and ohmic losses in the electrolyte [5].
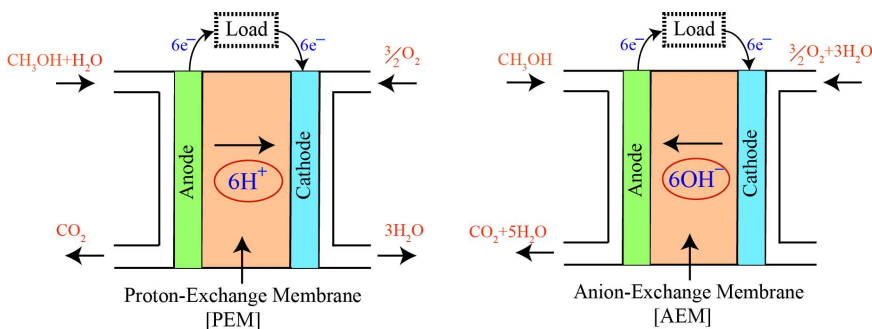
Figure 2.1 Schematic of a PEM-DMFC and AEM-DMFC.

Alkaline fuel cells (AFC) use the liquid electrolyte solution of potassium hydroxide (KOH) because it is the most conducting of all alkaline hydroxides. [1]. The major drawback of AFC is that KOH electrolyte is very sensitive to CO_2 that forms carbonates crystals such as K_2CO_3 which then precipitate in the cell. Another disadvantage is related to the amount of liquid electrolyte that may cause electrode flooding or drying [1]. Later on, advances in PEMFC brought the idea of

using a solid electrolyte for AFC to replace KOH with anion-conducting polymer electrolyte. This led to an increasing growth in research on AFC over the last thirty years.

In AEM-DMFC, methanol is supplied at the anode, and oxygen along with water is supplied at the cathode. At the cathode, ORR produces hydroxide ions (OH^-) that migrate through the electrolyte towards the anode. At the anode, OH^- reacts with methanol to produce water and electrons:

Anode	$CH_3OH + 6OH^- \rightarrow CO_2 + 5H_2O + 6e^-$	$E_0 = 0.814$ V/SHE	(4
Cathode	$\frac{3}{2}O_2 + 3H_2O + 6e^- \rightarrow 6OH^-$	$E_0 = 0.399$ V/SHE	(5
Overall reaction	$CH_3OH + \frac{3}{2}O_2 \rightarrow CO_2 + 2H_2O$	$E_0 = 1.213$ V/SHE	(6
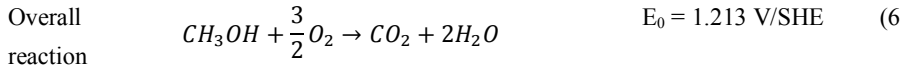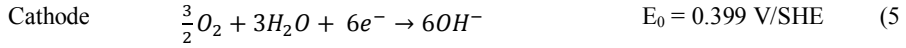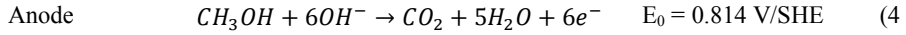
Even though the electrode reactions change in different media, the total cell reaction and thermodynamic potential of DMFC is the same. AEM-FC has several advantages compared to PEM-FC that makes them worth to study: 1) the kinetics of ORR and electro-oxidation of many liquid fuels are more facile in alkaline condition than in acidic one; 2) this allows the use of cheaper catalyst materials such as Ni, Ag or metal oxides rather than expensive Pt; 3) the electro-osmotic drag associated with ion transport suppress the crossover of liquid fuel, thereby allowing the use of more concentrated liquid fuels; 4) as water is consumed at the cathode in AEM-FC (unlike PEM-FC that water is produced), there is no problem with flooding issues.

There are some challenges which need to be addressed in AEMs. The mobility of OH^- is almost half that of H^+, leading to lower molar conductivity of hydroxide ions (198 S cm^2 mol^{-1}) compared to protons (349 S cm^2 mol^{-1}). Moreover, PEM-DMFC has been studied for longer time and currently can produce more than 10 times higher maximum power density than AEM-FC, due to the more mature technology development [6].

2.2 DMFC components

Fuel cell operation consists of complex phenomena occurring in various components. Figure 2.2 shows bipolar plate and flow channels, diffusion layer, membrane and a catalysts layer. Membrane electrode assembly (MEA), the heart of the fuel cell, comprises the membrane together with both catalyst layers.
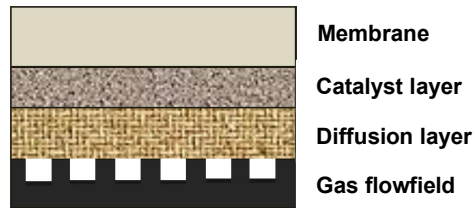

Figure 2.2. Schematics of fuel cell components.

Flow channels are located within the bipolar plates and distribute the reactants and remove byproducts. Bipolar plates provide mechanical support and conductive passages for both heat and electron transport. Insufficient supply of reactants will lead to starvation, reducing cell performance and stability degradation [7]. Conventional diffusion layer consists of a thin microporous carbon layer on a sheet of macroporous carbon paper or cloth. The diffusion layer is sandwiched between the catalyst layer and the flow channels and plays multiple roles: electrical connection between the bi-polar plate and the electrode, passage for reactant transport and heat/water removal, mechanical support to MEA and protection of the catalyst layer from corrosion or erosion caused by flows or other factors [8].

Ion exchange membranes generally consist of a polymer backbone and charged groups. The properties of the polymer backbone dominate the mechanical, chemical and thermal stability while the type of ionic groups and their concentration influence the ion exchange capacity, ionic conductivity and transport number. The presence of water is necessary for an efficient conductivity by enhancing the mobility of the ions. However, excessive water content results in decrease in mechanical stability and ionic conductivity [1]. Nafion® introduced by Dupont in 1967, is by far the most widely used protonic conductive polymer for PEMFCs. It contains hydrophobic polytetrafluoroethylene (PTFE, Teflon) backbone terminated with hydrophilic sulfonic acid groups for proton transport [9].

In AEMs, the ionic groups can be ammonium, phosphonium or sulfonium groups; among them, membranes containing ammonium groups exhibit the highest stability in alkaline media [10]. Commercial AEMs are still at an early stage of development and there are a number of challenges that must be overcome for their application in the fuel cell. One of the most important concerns in hydroxide-conducting membranes is the lower ion conductivity (10 times) compared to PEMs (0.1 S/cm). The weak basicity of the quaternary ammonium groups associated with the lower mobility of OH^- compared to H^+ limit the ion conductivity of AEMs. Another challenge is the stability of the membrane at high pH condition. This requires identifying the degradation mechanism that takes place in the alkaline medium.

The catalytic reactions take place in the catalyst layers which contributes significantly to the fuel cell cost. Different strategies have been proposed to reduce the cost of catalyst layer; that is alloying Pt with either less expensive precious metals (Ru, Pd) or non-precious metals (Co, Ni, Fe, Mn, Cr) [11, 12]. Another strategy is by optimizing the Pt loading and particle size distribution. In this context, using support materials with high surface is considered to achieve catalysts with high catalytically active surface area. A good support material must have sufficient electrical conductivity to conduct electrons properly. Moreover, it should have high percentage of mesopores in the range of 20-40 nm to provide enough surface area for the catalyst particles and ionomer, and to enhance the diffusion of chemical species through the catalyst layer network [13]. On this basis, different carbon nanomaterials have been addressed in the field of fuel cell electrodes.

2.3 Carbon nanomaterials

2.3.1 Carbon black

They are usually produced by pyrolysis of hydrocarbons such as natural gas or oil fractions taken from petroleum processing [14]. There are many types of carbon blacks (CB) such as Vulcan XC-72, Acetylene black, Ketjen Black, etc. CB consists of spherical particles of graphite with para-crystalline structure and diameter less than 50 nm that may aggregate to form agglomerates of around 250 nm (Figure 2.3). Each crystallite consists of several turbostratic layers with inter-spacing of 0.35-0.38 nm [15, 16]. Vulcan XC-72 is the most commonly used carbon black as catalyst support because of its high surface area (~250 m^2 g^{-1}), low cost and availability. However, this material still suffers from some problems such as:

- Presence of organo-sulfur impurities.

- Deep micropores: catalyst nanoparticles are trapped in micropores and become inaccessible to reactants and Nafion, thus not contributing to the electrochemical activity.

- CB is unstable under the highly acidic/alkaline conditions of fuel cells, resulting in corrosion of the carbon support and detachment or aggregation of catalyst nanoparticles.

Within this context, different alternative carbon nanostructures have been tailored and investigated in order to meet the demands of suitable catalyst support for fuel cells.
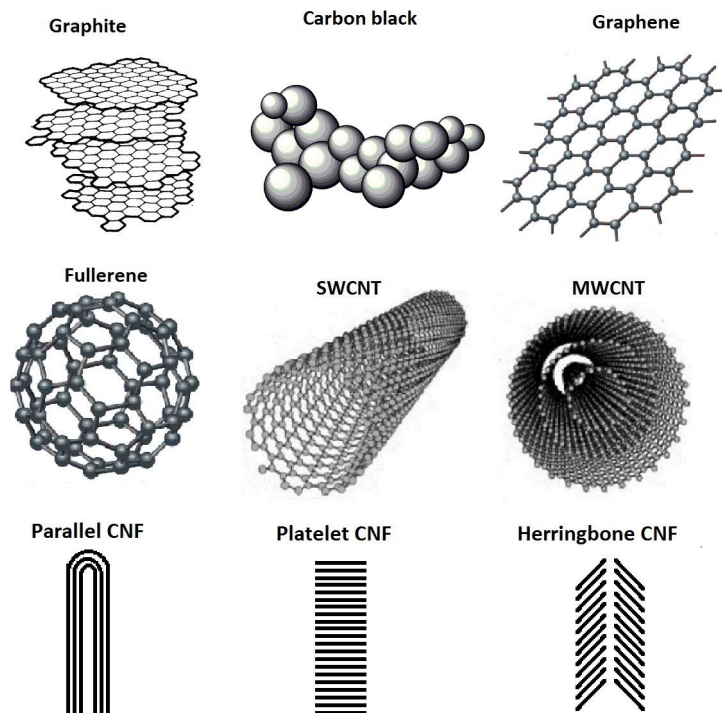

Figure 2.3. Allotropes of carbon nanomaterials.

2.3.2 Fullerenes

Fullerene was discovered in 1985 and refers to any type of closed hollow carbon molecule that forms either a sphere-like (buckyballs) or cylinder (buckytubes). The smallest member of the fullerene family is C20, and the most stable (C60) consists of 60 carbon atoms forming 20 hexagons and 12 pentagons as shown in Figure 2.3 [15, 17].

2.3.3 Graphene

Graphene (shown in Figure 2.3) is a one atom-thick layer of hexagonal sp^2 hybridized carbon atoms and was discovered in 2004. The 2-D planar structure of the carbon sheet allows both the edge planes and basal planes to interact with the catalyst nanoparticles. The fascinating singular properties of graphene such as high surface area (theoretical value, 2630 m^2 g^{-1}), high thermal conductivity and strong Young's modulus (~1TPa) have made graphene an excellent choice for various applications, in particular in the field of energy conversion and storage [18, 19].

Graphene nanosheets (GNS), with their high electron transport, 2-D crystal lattice and large area provide a continuous electron transport channel, and enhance the Pt utilization and activity. In many scientific reports graphene oxide (GO) has been used to support Pt nanoparticles, due to oxygen-containing functional groups on both basal planes (epoxy and hydroxyl groups) and edge planes (carbonyl and carboxyl groups). They are usually not single-layer and the presence of oxygen functional groups can act as anchoring sites to attach nanoparticles and enhance the uniform distribution [20, 21].

2.3.4 Carbon nanotubes

Carbon nanotubes can be generally classified as single-walled carbon nanotubes (SWCNT) and multi-walled carbon nanotubes (MWCNT) (illustrated in Figure 2.3). SWCNTs are made of one rolled graphene sheet containing sp^2 hybridized carbon atoms and closed by two caps (semi-fullerenes). Moreover, based on the number of walls (spaced by 0.34 nm), CNTs can be double-walled (DWCNT), few-walled (FWCNT) and up to several tens of walls, so that the external diameter reach 100 nm or more. The inner diameter of SWCNTs may vary between 0.4 and 2.5 nm and the length from few microns to millimeters. Typically, the surface area of SWCNT range between 400 and 900 m^2 g^{-1} (micropore volume, 0.15-0.3 ml g^{-1}) whereas for MWCNT it is about 200-400 m^2 g^{-1} [13]. CNTs have also extraordinary mechanical resistance with Young modulus in the order of TPa and tensile strength about 250 GPa. In addition, their thermal stability is considerable. Thermogravimetric analysis (TGA) showed that in the case of highly purified SWCNT the maximum gasification rate is located at around 800 °C and for MWCNT at about 650 °C. It should be noted that the concentration of surface defects and the remaining metal particles from CNT synthesis can influence thermal resistivity of CNTs [22].

2.3.5 Carbon nanofibers

Carbon nanofibers (CNF), also named as graphite nanofibers (GNF), have very thin or no hollow cavity unlike CNT, and their diameters can reach 500 nm. GNFs are classified mainly based on the orientation of the graphene layers with respect to the axis. As shown in Figure 2.3, ribbon GNF has graphene layers parallel to the axis, platelet GNF with perpendicular graphene layers and herringbone with oblique layers to the axis. Herringbone GNFs are known to have intermediate features between parallel and platelet types. They exhibit higher catalytic activity than parallel and better stability than the platelet GNFs [23]. Generally, GNF has no micropores, but mesopore volume is around 0.5-2 ml g^{-1} and the surface area ranges from 10 to 200 $m^2 g^{-1}$ [22].

In addition to above mentioned materials, other types of CNMs have been applied as support for electrocatalysts such as mesoporous carbon [24], carbon aerogels [25], carbon nanohorns [26], nanocoils [27] and etc. As they are out of the scope of this thesis, they are not described in details here. In the next sections, the reactions occurring at the electrocatalyst layers are discussed.

2.4 Methanol Oxidation Reaction

Electrocatalysis of the MOR has proven to exhibit a complex reaction mechanism, being one of the main bottlenecks in the DMFC performance.

2.4.1 MOR in acidic condition

In acidic media, the reaction includes adsorption of methanol, C-H bond activation (methanol dissociation), H_2O adsorption and activation, and finally addition of oxygen to adsorbed carbon-containing intermediates to generate CO_2 [5]. The total oxidation mechanism can be summarized as a pattern of parallel reactions which either goes through CO intermediate (path1) or oxygen-containing species to form CO_2 (path 2), as shown in Figure 2.4 [28, 29].
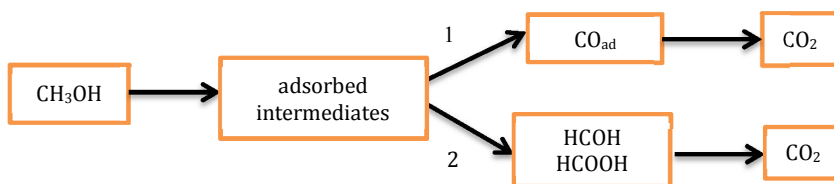
Figure 2.4. Simplified schematics of MOR mechanism.

The adsorption process takes place in several steps and requires several neighboring places at the surface, forming different species due to the dissociation of the molecule:

$$CH_3OH \rightarrow CH_2OH|_x + H + e^- \rightarrow CHOH|_{xx} + H + e^- \qquad (7$$
$$\rightarrow COH|_{xxx} + H + e^- \rightarrow CO|_x + H + e^-$$
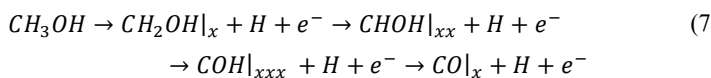
Here, x stands for a Pt-site. It was reported that formaldehyde (HCHO) and formic acid (HCOOH) can be formed from the intermediates CH_2OH and $CHOH$, respectively [30]. The oxidation

products of methanol at potentials between 0.5 and 0.6 V (RHE) are found to be CO_2, HCHO, HCOOH and $HCOOCH_3$ (methylformate). The yields of oxidation products depend on methanol concentration, temperature, electrode roughness and time of electrolysis [31]. Moreover, Pt surface structure has an effect on MOR. It was reported that the oxidation current followed the order as Pt(111) > Pt(110) > Pt(100), at a potential range from 0.45 to 0.65 V. However, methanol adsorption occurred at a higher rate at Pt(110) than Pt(111) [32].

MOR can also be affected by the anion of the supporting electrolyte. Perchloric ($HClO_4$) and sulfuric acids (H_2SO_4) are the most commonly used supporting electrolytes in acidic condition. However, much larger current was observed in $HClO_4$ than H_2SO_4, because of the stronger adsorption of sulfate species at Pt electrodes, which particularly hinders methanol oxidation [31].

2.4.2 MOR in alkaline condition

The MOR reaction mechanism in alkaline media is compared with acidic one in Table 2.1.

Table 2.1. MOR mechanism in acidic and alkaline media.

Acidic	*Alkaline*
$CH_3OH \rightarrow CO_{ad} + 4H^+ + 4e^-$	$CH_3OH + 4OH^- \rightarrow CO_{ad} + 4H_2O + 4e^-$
$H_2O \rightarrow H^+ + OH_{ad} + e^-$	$2OH^- \rightarrow 2OH_{ad} + 2e^-$
$CO_{ad} + OH_{ad} \rightarrow CO_2 + H^+ + e^-$	$CO_{ad} + 2OH_{ad} + 2OH^- \rightarrow CO_3^{2-} + 2H_2O$
Overall reaction	*Overall reaction*
$CH_3OH + H_2O \rightarrow CO_2 + 6H^+ + 6e^-$	$CH_3OH + 8OH^- \rightarrow CO_3^{2-} + 6H_2O + 6e^-$
E^0 = 0.016 V vs. SHE @ pH = 1	E^0 = -0.810 V vs. SHE @ pH = 14

From the above reactions, it can be seen that the pH of the supporting electrolyte is of great importance since H^+ and OH^- are involved in the reactions. The presence of OH^- also resulted in carbonate formation, hence the lower reaction potential. In alkaline media, the availability of OH_{ad} at relatively low potential might be the major reason for the higher activity toward MOR, leading to easier removal of CO_{ad}. The calculated rate constant in alkaline media (2.4 10^{-5} cm^3 s^{-1} mol^{-1}) is 20-fold higher than in acidic media (1.1 10^{-6} cm^3 s^{-1} mol^{-1}) [33]. In addition, the apparent activation energy in alkaline media is lower than in acidic media. For a fixed potential, the apparent reaction order in alkaline media is higher than in acidic condition. Overall, the better MOR activity of Pt-C in alkaline media is attributed to the faster methanol adsorption and availability of oxygen-containing species [34].

2.4.3 Catalyst promoter for MOR

At present, there is a general consensus that PtRu offers the most promising activity for the MOR in fuel cell conditions. In this binary catalyst, Pt is adsorbing and dissociating methanol while Ru is oxidizing the adsorbed residues at low potentials. In a simplified manner, one can describe the bi-functional mechanism as follows [29]:

Methanol adsorption:

$$CH_3OH_{sol} \rightarrow (CO)_{ad} + 4H^+ + 4e^- \qquad (8$$

(CO_{ad}) represents adsorbed CO on Pt or Ru.

Then both metals dissociate water to form adsorbed OH:

$$Ru + H_2O \rightarrow (OH)_{ad} + H^+ + e^- \qquad (9$$

$$Pt + H_2O \rightarrow (OH)_{ad} + H^+ + e^- \qquad (10$$
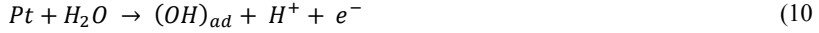
Finally, according to the Langmuir-Hinshelwood (L-H) mechanism the adsorbed CO reacts with adsorbed OH to form CO_2. It is more likely that the final oxidation occurs between CO adsorbed at Pt and OH adsorbed at Ru. Based on L-H mechanism, CO must diffuse on the surface to the places where the OH partner is formed.

$$Pt(CO)_{ad} + Ru(OH)_{ad} \rightarrow CO_2 + H^+ + e^- \qquad (11$$
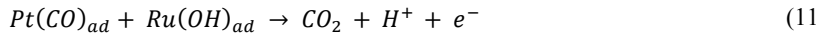
2.5 Oxygen Reduction Reaction

ORR in aqueous solutions occurs mainly by two pathways: the direct 4-electron reduction from O_2 to water, and the 2-electron reduction to hydrogen peroxide. In the fuel cell, the 4-e⁻ pathway is desired, because hydrogen peroxide (produced from the 2-e⁻ pathway) is commonly known to cause chemical degradation of membrane and catalysts [35]. The mechanism of the ORR is quite complicated and involves many intermediates, depending on the nature of the electrode material, catalyst and electrolyte. Table 2.2 shows the ORR processes in acidic and alkaline media with their corresponding thermodynamic electrode potential at standard conditions [36].

Table 2.2. The ORR process in acidic and alkaline media with thermodynamic electrode potential at standard condition.

Electrolyte	Pathway	ORR Reactions	E (V)
Acidic	4-e⁻ process	$O_2 + 4H^+ + 4e^- \rightarrow 2H_2O$	1.229
	2-e⁻ process	$O_2 + 2H^+ + 2e^- \rightarrow H_2O_2$	0.70
		$H_2O_2 + 2H^+ + 2e^- \rightarrow 2H_2O$	1.76
Alkaline	4-e⁻ process	$O_2 + 2H_2O + 4e^- \rightarrow 4OH^-$	0.401
	2-e⁻ process	$O_2 + H_2O + 2e^- \rightarrow HO_2^- + OH^-$	-0.065
		$HO_2^- + H_2O + 2e^- \rightarrow 3OH^-$	0.867

2.5.1 ORR mechanism on carbon materials

It is generally acknowledged that the quinone groups are responsible for the ORR activity on carbon materials. These groups on a carbon electrode can catalyze a 2-e⁻ reduction of O_2 to H_2O_2 in acidic media. In this mechanism, the superoxide intermediate (Q-O_2^-) reacts with a second electron and protons from water to form hydrogen peroxide. In alkaline media, the main product is hydroperoxide anion (HO_2^-) [37, 38].

$$Q + e^- \rightarrow Q^{\cdot-} \tag{12}$$

$$Q^{\cdot-} + O_2 \rightarrow Q - Q_2^- \tag{13}$$

$$Q - Q_2^- + 2H^+ + e^- \rightarrow Q + H_2O_2 \tag{14}$$

2.5.2 ORR mechanism on Pt-catalyst

The catalytic ORR is a multi-electron process with a number of elementary steps, but with only two products: H_2O_2 and H_2O. The simplified reaction scheme proposed by Wroblowa (Figure 2.5), appears to be the most effective model among others to describe the complex ORR pathway [39].
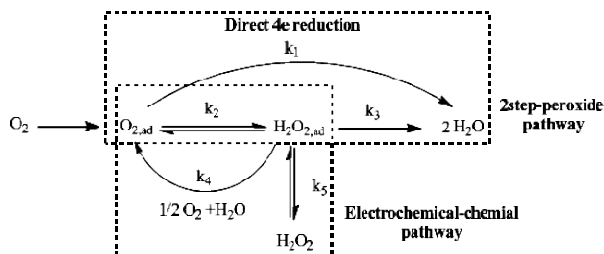

Figure 2.5. Simplified ORR scheme.

In this mechanism, O_2 can be either reduced electrochemically directly to water (direct 4-e⁻ reduction) with the rate constant k_1, or reduced to adsorbed hydrogen peroxide with the rate constant k_2 (2-e⁻ reduction). $H_2O_{2,ad}$ can be further electrochemically reduced to water with the rate constant k_3. Then, it can be chemically decomposed to $O_{2,ad}$ on the electrode surface (k_4), or desorbed into the electrolyte solution (k_5). Some experimental results suggest that a series pathway via an $(H_2O_2)_{ad}$ intermediate is the most possible pathway on carbon catalysts. RRDE measurements show that on a Pt surface, ORR is mostly a 4-e⁻ transfer process to H_2O both in acidic and alkaline electrolytes. That is, only a very small amount of H_2O_2 could be observed during ORR, and the electron transfer number is close to 4.

The thermodynamic potential of ORR is so high (1.23 vs. NHE at standard conditions) that no electrode materials can remain pure and they undergo oxidation, and it changes their surface properties. Therefore, even for the most catalytically active electrode, Pt group metals, the measurable currents are obtained usually below 1V. At high potential, the following reaction occurs on Pt electrode:

$$Pt + \frac{1}{2}O_2 \rightarrow PtO \qquad\qquad E^0 = 0.88 \text{ V} \tag{15}$$

Thus, in the presence of O_2, Pt surface is a mixture of Pt and PtO. Therefore, a steady-state open circuit potential (OCP) of 1.23 V is rarely observed, due to the formation of PtO. Rather, the steady-state rest potential of Pt electrode in O_2-saturated 1M H_2SO_4 is 1.06 V, a mixed value of the thermodynamic potential of O_2/H_2O and Pt/PtO, because the two reactions occur: O_2 reduction and Pt oxidation [36].

3 Methods

3.1 Specifications of carbon nanomaterials

Different types of carbon nanomaterials were used in the present thesis both as carbon support for PtRu nanoparticles and nitrogen doped electrocatalysts. Figure 3.1 shows representative TEM micrographs of Carbon black (Vulcan), GNFs and FWCNTs.
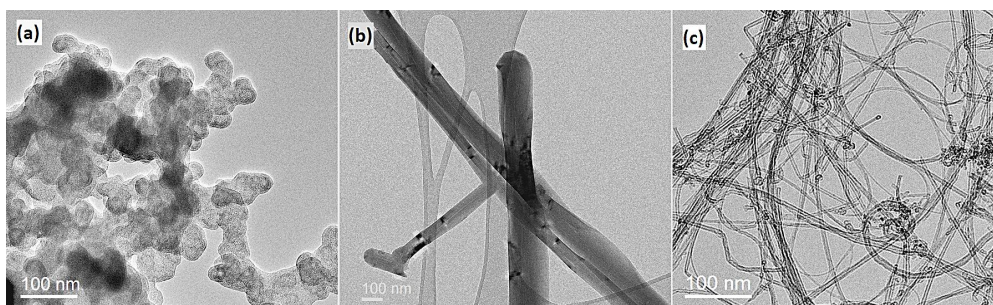

Figure 3.1. TEM micrographs of a) Vulcan, b) GNFs, c) FWCNTs.

Vulcan XC-72, a powdered carbon black was received from Cabot Corporation. Vulcan has a turbostratic structure with a particle size of 30-50 nm and 154 m^2g^{-1} BET surface area. GNFs were provided by Showa Denko (Japan), with the trade name of VGCF^{TM}. GNFs have an average diameter of 150 nm and 10 μm length with very low surface area (17 $m^2 g^{-1}$). GNFs were highly graphitized by annealing at elevated temperatures above 2800 °C. FWCNTs contain 2-5 graphitic walls up to 6 nm diameter and about 1 μm length, with a high surface area of 449 m^2g^{-1}. The specifications of the carbon nanomaterials are summarized in Table 3.1.

Table 3.1. Specifications of carbon nanomaterials.

CNM	Av. Diameter (nm)	Length (μm)	Surface area (m^2g^{-1})	Raman (I_D/I_G)	Supplier
Vulcan	30-50	--	154	1.2	Cabot Co.
GNF	150	10	17	0.37	Showa Denko
FWCNTs	6	1	449	0.43	Aalto University

FWCNTs were synthesized in house by chemical vapor deposition (CVD) through decomposition of methane (CH_4) diluted with hydrogen (H_2) on MgO supported Co-Mo catalyst at 950 ºC [40]. After synthesis, residual metal catalysts were removed from FWCNTs by washing in hydrochloric acid (HCl), rinsed properly with deionized water and dried in vacuum.

Graphene nanoplatelets (GNPs) were purchased from Cheap Tubes Inc. (GNPs Grade 3). According to the supplier's specifications, GNPs has an average thickness of 8-12 nm and typical particle diameter less than 2 microns with surface area in the range of 600-750 m^2/g. The morphology of GNPs is shown in the SEM image in Figure 3.2.
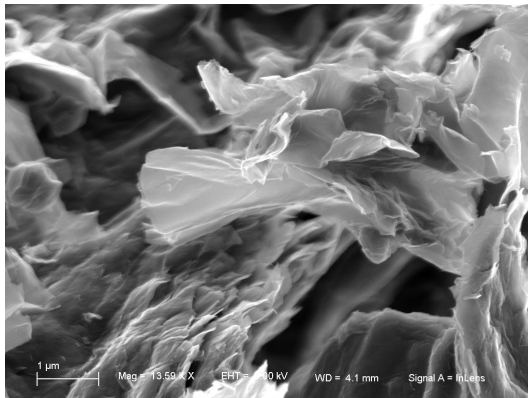

Figure 3.2. Surface morphology of GNPs, a) SEM

3.2 Electrochemical characterization

3.2.1 Electrochemical cell

The most common electrochemical set-up is the 3-electrode cell system consisting of a working electrode (WE), a reference electrode (RE) and a counter electrode (CE) (Figure 3.3). The WE is the electrode where the electrochemical reaction takes place and is commonly made of inert materials such as Au, Ag, Pt or glassy carbon. The CE supplies the current required for the reaction at the WE. It is made of inert materials and usually does not participate in the electrochemical reaction. As the current flows between the WE and CE, the total surface area of CE must be higher than the area of the WE so that it will not be a limiting factor in the kinetics of the electrochemical process. The RE, which is kept in a separate container connected to the cell through Luggin capillary, has a stable potential so that the potential at the WE can be measured and controlled with respect to that of the RE. The high stability of the RE potential is usually reached by employing a redox system with constant concentrations of each participants of the redox reaction. In the electrolyte phase, the movement of ions (typically H$^+$, Na$^+$, K$^+$, Cl$^-$ in aqueous or non-aqueous solvents) is responsible for the transfer of charge [41].

Different types of RE are used in electrochemistry. The standard hydrogen electrode (SHE), or normal hydrogen electrode (NHE) is generally accepted as international standard ($Pt/H_2/H^+$). Other commonly used REs are saturated calomel electrode (SCE) ($Hg/Hg_2Cl_2/KCl$) with a potential of 0.242 V vs. NHE, and silver-silver chloride electrode (Ag/AgCl/KCl) with a potential of 0.197 V vs. NHE. Other REs are mercury/mercurous sulfate ($Hg/HgSO_4$) and mercury/mercury oxide (Hg/HgO, 0.64 V vs. NHE).
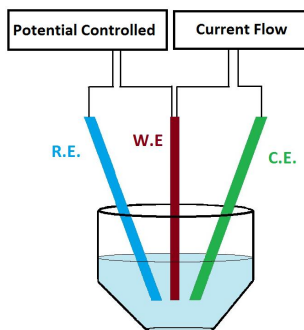

Figure 3.3. Schematic of a three-electrode cell.

In characterization of fuel cell electrocatalysts, common electrolytes for acidic conditions are sulfuric (H_2SO_4) and perchloric acid ($HClO_4$). Because sulfuric acid dissociates to sulfate ions, it resembles the sulfonic groups of Nafion ionomer. However, sulfate anions absorb more strongly than perchlorate ions on Pt active sites inhibiting the methanol adsorption and oxidation [31]. In alkaline medium, NaOH or KOH are commonly used as electrolytes. However, it is reported that the non-covalent interactions between the hydrated Na^+ cations and adsorbed OH species are stronger than with hydrated K^+ cations so that the $OH_{ad}^-M^+(H_2O)_x$ clusters block the active sites for the electrocatalytic reaction [42]. In the present thesis, 0.1 M $HClO_4$ and 0.1M KOH that form weekly adsorbing species were used as electrolytes for the characterization of MOR at PtRu-C catalysts (in acidic condition), and the ORR at N-doped CNMs (in alkaline condition), respectively.

3.2.2 Electrode preparation

Catalyst inks were prepared by dispersing the catalyst powders in a solvent containing the ionomer by magnetic stirring and ultrasonication. PtRu-catalysts on different carbon supports were mixed properly with isopropanol and Nafion® (proton exchange ionomer) and kept in ultra-sound bath. In case of N-doped catalyst powders, ethanol and FAA3 (anion exchange ionomer) were used. A drop of the ink was carefully deposited on polished glassy carbon electrodes (GCE, 0.196 cm^2) and dried in room conditions. The half-cell electrochemical measurements were performed using glassy carbon electrodes modified with the catalysts as working electrode, a platinum coil counter electrode and a reference electrode. The reference electrode for characterizing PtRu-CNMs was a saturated calomel electrode (SCE) in 0.1 M $HClO_4$ electrolyte. An Ag/AgCl reference electrode was used for characterizing the N-doped CNMs in 0.1 M KOH electrolyte.

3.2.3 Cyclic Voltammetry

Cyclic voltammetry (CV) is one of the most useful electrochemical techniques. It can provide quick information about the electrocatalytic activity of a catalyst towards an electrochemical reaction. In CV, the WE potential is swept between two values and back at a fixed scan rate. The onset potential and peak current reveal the activity of a catalyst. In chronoamperometry and chronopotentiometry, respectively the voltage and the current at the WE is stepped to a certain value and the resulting current/potential from the faradic process is monitored over time. These transient methods are useful to provide information about the degradation process and poisoning of the electrocatalyst.

3.2.4 Rotating disk electrode measurements (RDE)

RDE is a useful method to investigate the activity of an electrode toward the ORR. In a RDE system, the electrode is rotating so that a continuous laminar flow of solution is flung toward and across the electrode (Figure 3.4). Thanks to electrode rotation, mass transport of the species is almost completely convection, allowing study of mass transport and kinetic parameters of the electrochemical reaction [43].
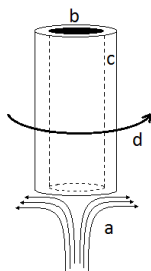
Figure 3.4 Solution movement caused by rotation of RDE: a) flow of electrolyte, b) glassy carbon electrode, c) RDE body, d) direction of the electrode rotation.

The overall current density (j) in RDE measurements can be evaluated by the Koutecky-Levich (K-L) equation:

$$\frac{1}{j} = \frac{1}{j_k} + \frac{1}{j_d} \tag{16}$$

Where j_k is the kinetic current density, and j_d is the diffusion-limited current density, which for the case of ORR can be expressed as:

$$j_k = nFK_{O_2} C_{O_2} \Gamma_{catalyst} \tag{17}$$

$$j_d = 0.62nFD_{O_2}^{2/3} v^{-1/6} C_{O_2}^b \omega^{1/2} \tag{18}$$

F is the Faraday constant (96486.4 C mol^{-1}), D_{O2} is the diffusion coefficient of oxygen in the electrolyte, C_{O2} is the concentration of oxygen, v is the kinematic viscosity of the electrolyte, and ω is the electrode rotation rate (rad s^{-1}). Table 3.2 lists the parameters for common electrolytes [11].

The number of transferred electrons (n) can be obtained from the slope of extrapolated lines at different potentials in K-L plots (j^{-1} vs $\omega^{-1/2}$).

Table 3.2. Parameters for common electrolytes for RDE data analysis.

Experimental condition	D_{O2} (cm² s⁻¹)	v (cm² s⁻¹)	C_{O2} (mol cm⁻³)
0.1 M KOH, 25°C, 1 atm O_2	1.9×10^{-5}	1.0×10^{-2}	1.2×10^{-6}
0.1 M NaOH, 25°C, 1 atm O_2	1.65×10^{-5}	1.1×10^{-2}	8.4×10^{-7}
0.1 M HClO₄, 20°C, 1atm O_2	1.67×10^{-5}	0.89×10^{-3}	1.18×10^{-6}
0.1 M H₂SO₄, 25°C, 1atm O_2	1.4×10^{-5}	1.1×10^{-2}	1.1×10^{-6}

3.2.5 Rotating ring disk electrode measurement (RRDE)

RRDE measurements are very useful for elucidating the ORR mechanism. A RRDE consists of a central GC disk and a Pt-ring separated by a non-conductive barrier, as shown in Figure 3.5. In the case of the ORR, the disk electrode is biased at a potential at which oxygen reduction occurs and intermediate products are flung to the Pt-ring while the RRDE is rotating. At the disk, the ORR can take place via a 2 or 4-electron pathway and the generated intermediates such as H_2O_2 (in acidic media) or H_2O^- (in alkaline media) are further oxidized at the ring that is kept at a fixed potential.
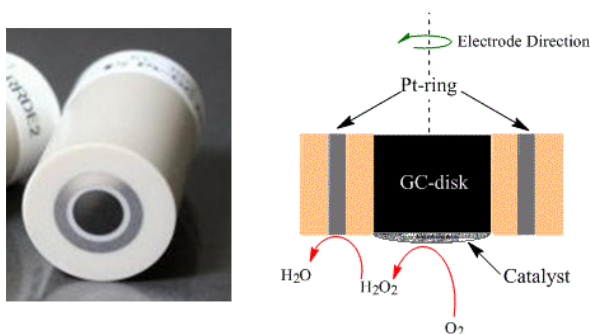
Figure 3.5. RRDE (GC-disk and Pt-ring): photograph and schematics of the reactions taking place during ORR at the GC disk and Pt-ring in alkaline media.

In RRDE measurements, the number of transferred electrons (n) and percentage of H_2O_2 generated can be calculated from the following equations:

$$n = \frac{4\,I_d}{I_d + \frac{I_r}{N}} \tag{19}$$

$$H_2O_2\,\% = \frac{4 - n}{2} \times 100 \tag{20}$$

where N is the collection efficiency (usually ~0.24), I_d and I_r are the currents measured at the GC-disk and the Pt-ring, respectively [36].

25

3.3 Fuel cell measurements

The fuel cell used in Publication I, III and IV is a single-cell with serpentine flow channel by Fuel Cell Technologies with active surface area of 7.29 cm^2. Figure 3.6a shows the cell stack, MEAs, Teflon® gaskets for isolation, and the diffusion layers which are a type of carbon cloth with 10 and 60% Teflon® dispersion, respectively for the anode and the cathode side.

In Publication II, DMFC measurements were carried out using microfabricated silicon chips with an integrated silicon nanograss diffusion layer (Figure 3.6 b&c). Silicon nanograss is a quasi-random array of needle-like silicon structures, about 2 µm tall and 200-300 nm wide at the base. Using Si-nanograss has some benefits. The simple fabrication makes it possible to directly fabricate them on the flow fields or the membrane. In addition, Si-nanograss with much smaller thickness than the traditional carbon cloth (200-400 µm) is advantageous to make the MFC with smaller dimension which is a plus point for microelectronic applications.
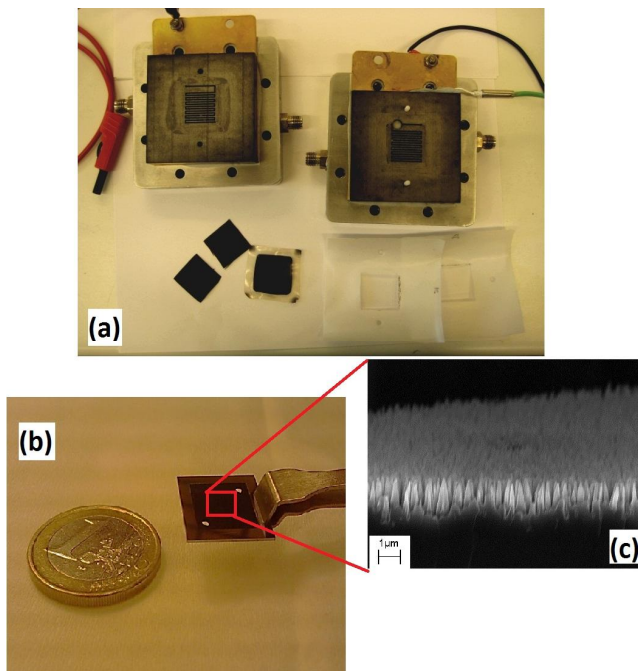
Figure 3.6. a) Fuel cell stack (7.29 cm^2), carbon cloths, MEAs and Teflon gaskets [taken with permission from A.Santasalo-Aarino doctoral dissertation], b) Si-microfabricated chip with c) silicon nanograss diffusion layer [Pub.II].

3.3.1 Membrane Electrode Assembly

The common method for fabricating electrodes for fuel cell testing came from a breakthrough in Los Alamos National Laboratory (LANL) by Raistrick [44]. The method was called catalyst-ink technique where the ink contained dissolved Nafion at the surface of the porous catalyst material. Once the solution and the electrodes were passed to the membrane, the Nafion provided an ion-conducting path from membrane to the metal catalyst particles. Later, M.S. Wilson invented a

method for fabricating reproducible thin-film electrodes bonded to the membrane, the so-called membrane electrode assembly (MEA). In combination, these techniques have dramatically lowered the required metal loading by a factor of more than 20 while simultaneously improving performance. Other fabrication methods for MEAs have been developed recently such as electrodeposition, sputter deposition, pulsed laser ablation, dry spray, and layer-by-layer methods [45].

In this thesis we have used the catalyst-ink method for preparing MEAs and the ionomer content is reported as the weight percentage of ionomer to the whole catalyst layer (CL) dry weight. The experimental protocol is as follows: first the membranes are pretreated. For the PEM fuel cells, the Nafion membrane was boiled in 5% H_2O_2, and 0.5 M H_2SO_4 and finally twice in deionized water. The catalyst inks were prepared by mixing catalysts with Nafion ionomer and isopropanol. Then the slurry was painted on the Nafion membrane by an airbrush and dried in vacuum. The anode electrode was prepared using PtRu-CNM materials with metal loadings about 1 ± 0.2 mg cm^{-2} and at the cathode a commercial Pt-carbon black (60 wt.% Pt, Alfa Aesar) with 2 ± 0.2 mg cm^{-2} catalyst loading (Pub.I, II and III).

In the case of AEM fuel cell (Publication IV), the protocol was: first a FAA3 (Fumatech) membrane was dipped in 0.5 M NaOH for 1 h for ion-exchange and then twice in deionized water. Catalyst inks were prepared by dispersing catalysts with FAA3 ionomer solution and isopropanol. FAA3 ionomer is received as 12 wt. % dissolved in N-methyl-2-pyrrolidone (NMP). Therefore, the ink was sprayed on the microporous carbon layer at around 140ºC to evaporate NMP. The cathode inks contained N-FWCNTs with 2.2 ± 0.3 mg cm^{-2} loading. The anode was made of a commercial PtRu catalyst-supported on high surface area carbon (40 %wt. Pt, 20 %wt. Ru, Alfa Aesar) with 3 ± 0.2 mg cm^{-2} metal loading.

3.3.2 Polarization curves

DMFC measurements were carried out at a controlled temperature by feeding 1M methanol solution to the anode and dry oxygen to the cathode. Before the experiments fuel cells stabilized with the steady methanol and air flow overnight and then the polarization curves were measured. The polarization curve describes the relationship between the electrode potential and the current density, recorded by either holding the electrode potential and measuring the current response, or holding the current density and recording the stable potential response. In fuel cell performance, high current density is expected at high cell voltage, which gives maximum power density. The polarization curve starts from the open circuit voltage (OCV). As the cell voltage decreases from the OCV, at a certain rate (for instance, 1mV/s) the generated current density is measured. OCV is the voltage when no current follows through the external circuit while the reactants are circulating. The output power of the cell (mWcm^{-2}) can be plotted as the product of voltage and current density.

3.3.3 Stability tests

In Publications I, II the stability of PtRu-catalysts was investigated by chronoamperometric measurement (constant voltage) at 0.4 and 0.2 V, respectively. In this method, the potential of the cell is fixed but the potentials of anode and cathode are changing. In Publication III chronopotentiometric measurement (constant current) was carried out at 27 mA cm^{-2}. In the constant current measurement, the fuel consumption and product generation stay constant during the measurement. This method is advantageous because, unlike the former method, the performance changes are due to the fuel cell component structure, not related to the flow.

Further, the degradation of the catalyst particles and the changes in the electrode layer structure after the long-term measurements were assessed by different ex-situ microscopy techniques.

3.3.4 Electrochemical Impedance Spectroscopy (EIS)

In electrochemical impedance measurement, a small amplitude AC signal is imposed to the fuel cell, and the AC voltage/current response is analyzed to determine the impedance (resistive, capacitive and inductive behavior) at that particular frequency. Physico-chemical processes occurring in the cell have different time-constants and therefore are exhibited at different AC frequencies. EIS can be used to identify and quantify the impedance associated with various processes when conducted over a broad range of frequencies. In Publication III the spectrum of the whole cell was measured from 100 to 10 kHz using a 10 mA sinusoidal signal. EIS is a good technique to identify the sources of losses in the cell.

3.4 Physico-chemical characterization

Scanning electron microscopy (SEM) was carried out with a field emission JEOL microscope JSM-7500FA equipped with an energy dispersive X-ray spectrometer (EDXS). Transmission Electron microscopy (TEM) was performed using a Tecnai 12 BioTwin with LaB6 gun at 120 kV. High resolution TEM (HR-TEM) was conducted with a JEOL double Cs-corrected microscope (JEM-2200FS) operated at 200 kV.

X-ray photoelectron spectroscopy (XPS) was carried out with a Surface Science Instruments SSX-100 ESCA spectrometer using monochromatic AlKα X-rays and an electrostatic hemispherical analyzer. The spectra were recorded with pass energy of 100 eV and an X-ray spot size of 600 µm. X-ray diffraction (XRD) spectra were obtained by a Bruker D8 advanced X-ray diffractometer using Cu-Kα radiation and a Lynx Eye fast detector with scan conditions of 2 s/0.03°. Brunauer-Emmett-Teller (BET) surface area measurements were done by N_2 adsorption-desorption isotherms at 77 K with a FlowSorb 2300II instrument by Micromeritics. Raman analysis was performed using a Horiba LabRAM HR spectrometer equipped with CCD camera and a 633 nm laser beam. Thermal gravimetry analysis (TGA) measurements were carried out with a TA-Instrument Q500 TGA using a temperature range of 30-800 °C at a heating rate of 10 °C min^{-1} under nitrogen.

4 CNMs as catalyst support

4.1 Preparation of CNMs as support

CNTs and CNFs have received a lot of attention for fuel cell applications among other carbon nanomaterials. These highly crystalline nanocarbons have shown superior performance and durability due to their chemical stability, high mechanical strength and electrical conductivity, compared to the classical carbon black supported catalysts [46-48]. High resistance to carbon corrosion is a fundamental benefit of utilizing highly graphitized carbon nanofibers and nanotubes rather than traditional carbon black for catalyst support when operating at elevated temperature and highly oxidizing environment in fuel cells [49]. The interaction between the surface of the tubular support and the catalyst has an influence on electrode durability. The highly tailored GNF structure was shown to enhance the activity of the catalyst due to specific crystallographic orientations of Pt crystal [50]. In addition, negligible micropores content in GNFs is an advantage as it allows higher catalyst utilization and enhanced mass transport [51].

In the present thesis, FWCNTs and GNFs were used as PtRu catalyst support for the DMFC anode, and their influence on durability was compared with that of traditional carbon black support. FWCNTs, as an intermediate between SWCNTs and MWCNTs, render an appropriate combination of structural perfection, high surface area and electronic properties for catalysis application [52].

Carbon nanotubes and fibers are highly hydrophobic and inert in nature and it is difficult to achieve a high dispersion of metal particles because the nanoparticles do not easily find anchoring sites on the nanotube walls. In order to overcome this issue, anchoring sites must be formed by functionalizing the surface. Functionalization using oxidizing agents is one of the common methods in order to introduce oxygen-containing functional groups at the surface of CNMs. The oxidative treatment makes them more hydrophilic and enhances their wettability in polar solvents which is beneficial in catalyst preparation and use. Oxygen functional groups also work as anchoring sites for the deposition of metal particles and large molecules [53]. Different approaches have been reported for the oxidative treatment of CNMs: in gas phase (by exposure to ozone, carbon dioxide and oxygen plasma), and in liquid phase (by using acids, hydrogen peroxide and permanganate) [54-56]. The most common approach is the oxidation in liquid phase using nitric acid, sulfuric acid or their mixtures. This method has been applied using a variety of acid concentrations, temperature and treatment duration. In this work, GNFs and FWCNTs were treated in refluxing conditions with 2 M HNO_3/1 M H_2SO_4 (1:1) mixture at 120 °C. GNFs were treated for a longer time (6 h) than FWCNTs (4 h), as they are more graphitized and their walls are more inert to anchor metal particles.

4.2 Preparation of Pt-based catalysts on CNMs

Several methods have been proposed for preparation of fuel cell electrocatalysts. The physiochemical properties of electrocatalysts, particle size and crystallinity, significantly influence their activity. Therefore, several synthesis methods have been proposed to control the catalytic properties [57, 58]. They are mainly divided to two categories: physical and chemical techniques.

Physical methods include high-energy ball milling, spray pyrolysis, vapor deposition and plasma sputtering. During ball milling process, powder particles are subjected to intense mechanical deformation via impact of balls inside an air-tight crucible. Synthesis of PtRu catalysts with this technique can be done in combination with a leaching procedure [59]. In spray pyrolysis, the metal salts (Pt and Ru precursors) are mixed in a solvent with a colloidal suspension of the carbon support and converted into an aerosol through an atomizer. The aerosol is carried by a gas flow into a tube furnace. The solvent evaporates and the precursors are thermally or chemically converted into their final form on the surface of the carbon support [60].

In vapor deposition technique, Pt and Ru precursors are sublimed at high temperature (~220 °C) in a vacuum chamber that contains the carbon support substrate. Subsequent cooling of the chamber results in deposition of the metal clusters onto the substrate surface. Then the precursor impregnated substrate is kept at high temperature (~300 °C) under nitrogen atmosphere to decompose and yield PtRu bimetallic nanoparticles [61]. In plasma sputtering method, Pt and Ru targets are faced to the substrate (carbon support) at a specific distance, in a vacuum chamber. The biased targets are bombarded with heavy gas (energetic argon atoms) created by inductive plasma. Metal atoms ejected from the targets cross the plasma to deposit onto the substrate [62].
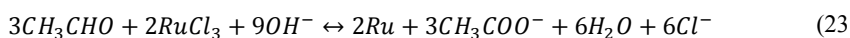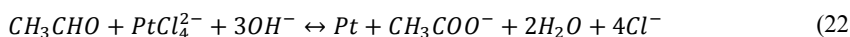
Chemical methods usually consist of reduction of the metal salts in solution, and include electrochemical deposition, microemulsion, impregnation, colloidal and polyol techniques. Electrodeposition has some advantages such as simplicity of production, high purity of deposition, easy control of the deposition condition and the loading mass. Disadvantage of the method is the formation of agglomerates [3]. Electrochemical methods for deposition of Pt nanoparticles have been reported either using constant current/potential or pulse current/potential methods[63].

Microemulsion method for nanoparticle preparation consists of nano-sized water droplets surrounded by an organic phase stabilized by surfactant (water-in-oil) [64]. The reduction step can be done either by adding a reducing agent or mixing with another microemulsion system containing the reducing agent. In order to remove the remaining surfactant, the sample is heat-treated under N_2 atmosphere. This method is advantageous in controlling the metallic composition and the particle size within a narrow distribution [14, 65]. Impregnation method includes deposition of metal precursors into a porous support, followed by a reduction step to turn them into metallic nanoparticles. Different types of precursors have been reported for the synthesis of PtRu electrocatalysts such as chloride and sulfite salts, carbonyl and amine complexes [14]. The reduction step can be done either in a liquid phase or in a gas phase using hydrogen flow at high temperature (>300 °C). The catalyst supports have great influence on metal precursor penetration,

distribution and the growth of nanoparticle size during the reduction step. [57]. This is simple method and easy to scale-up, however it is difficult to control the nanoparticle size and distribution especially at high catalyst loadings [66].

The colloidal method usually involves several steps. Bönnemann developed a method consisting of first stabilization of the PtRu particles using organic molecules/organoaluminum compounds to form colloids, then adsorption on high-surface area support followed by thermal treatment to remove the stabilizer shell [58, 67]. The long multi-step process and the use of expensive materials are disadvantages of this method. Moreover, the stabilizing organic materials remain on the surface of the metal colloids and should be removed prior to the application of metal particles for electrocatalysis. The necessary heat treatment for this aim causes sintering, phase separation and the distribution of metal particles, leading to lower catalytic performance [68]. In this respect, catalyst preparation via polyol method is preferred in this thesis, because of several advantages that are described below.

The polyol method uses a polyol such as ethylene glycol (EG) both acting as solvent and reducing agent. The advantage of this process is that it does not need any polymer stabilizer, although it can be used. The metal colloids are formed while metal ions are reduced by receiving electrons from the oxidation of ethylene glycol to glycolic acid. Glycolic acid is present in its deprotonated form (glycolate anion) in alkaline solution. It is believed that the glycolate anion acts as a stabilizer and adsorbed on the metal colloids. A following heat treatment below 160 °C allows removal of the organics from the metal surface while being low enough to avoid sintering of the particles [68]. The use of alkaline media is crucial parameter to control the particle size. It is reported that increasing NaOH concentration resulted in a decrease in nanoparticle size [69]. PtRu nanoparticles form through the following reactions as EG is heated [70, 71].

$$CH_2OH - CH_2OH \leftrightarrow CH_3CHO + H_2O \qquad (21$$
$$CH_3CHO + PtCl_4^{2-} + 3OH^- \leftrightarrow Pt + CH_3COO^- + 2H_2O + 4Cl^- \qquad (22$$
$$3CH_3CHO + 2RuCl_3 + 9OH^- \leftrightarrow 2Ru + 3CH_3COO^- + 6H_2O + 6Cl^- \qquad (23$$

As mentioned above, due to the interaction of –OH groups of EG with Pt ions the colloidal particles form, resulting in the oxidation of the alcohol groups to aldehydes. These aldehydes are not very stable and undergo further oxidation to glycolic and oxalic acids, respectively. These carboxylic acids may be further oxidized to CO_2 or carbonate in alkaline media. Glycolate ions are considered as stabilizer by forming chelate-type complexes via carboxyl groups. It is reported that the nanoparticle size is correlated to the concentration of glycolic anion, which in turn, is a function of the pH of the solution [69].

In Publications I, II, and III, PtRu nanoparticles were deposited on the carbon supports by reduction of the corresponding metal precursors using the polyol method (Figure 4.1). First the CNMs (100 mg) were dispersed in EG. Stoichiometric amount of K_2PtCl_4 and $RuCl_3$ were dissolved in EG/water and for target metal loading 30 wt. % (Pt:Ru 1:1 atomic ratio). Then the solution of metal dispersion was added to the carbon support suspension. A solution of 0.4 M NaOH and 0.04 M $NaBH_4$ was added dropwise under vigorous agitation and mixed properly. The

resulting suspension was kept in ultrasound bath for 2 h at 60 °C. Finally, the suspension was filtered, rinsed and dried in vacuum oven over night at 40 °C.
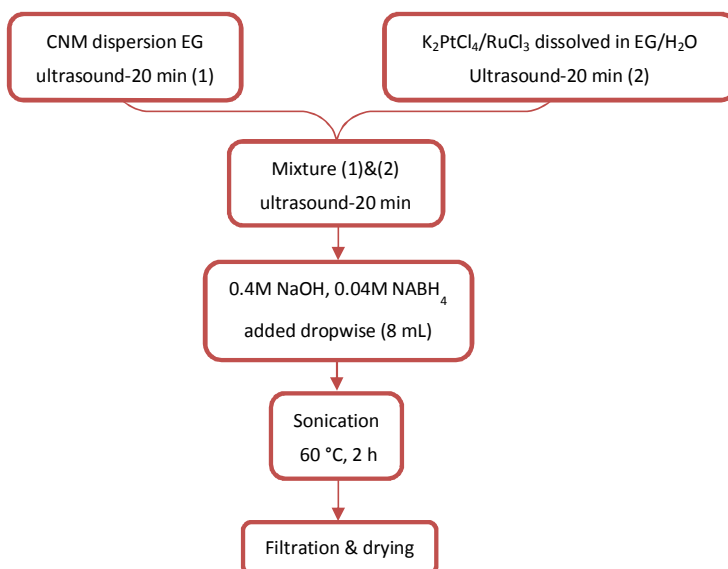

Figure 4.1 PtRu nanoparticle deposition on nanocarbon supports by polyol method

4.3 Characterization of PtRu-CNMs

After catalyst preparation, a physico-chemical characterization was done to ensure that metal particles with the desired loading, size and distribution were obtained over the carbon supports. EDXS analysis is a straightforward technique to estimate the metal content of the catalysts and it showed that the catalyst loadings was lower than the 30 wt. % target (Table 4.1). This is commonly observed in the literature and caused by preparation of the catalysts in solvent, since some loosely attached nanoparticles can be removed during the filtration process [70]. TEM microscopy of fresh PtRu catalysts supported on carbon supports were done to investigate the nanoparticle size and distribution (Figure 4.2).
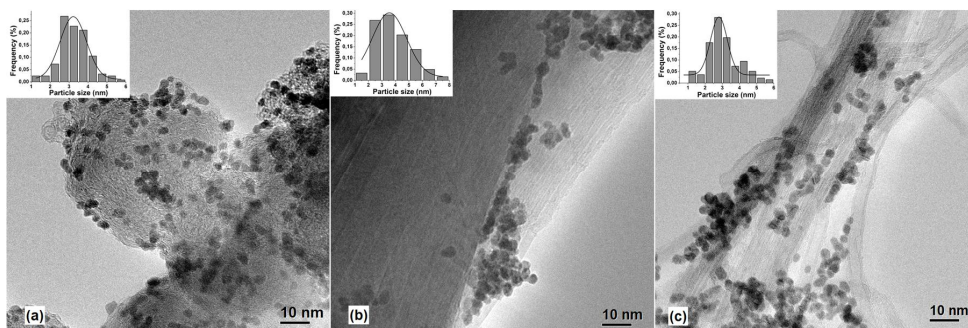

Figure 4.2. TEM micrographs; nanoparticle size distribution over carbon supports a) Vulcan, b) GNF and c) FWCNTs (Pub.II)

A quantitative analysis of the average nanoparticle size was done by counting almost 200 nanoparticles from HR-TEM images together with the Gaussian fitting on the histograms. Table 4.1 presents the nanoparticle size for the fresh samples used in both macro- and micro-DMFC. It can be seen that catalyst materials with comparable metal particle size (~3 nm) were obtained even though BET surface area, porosity and crystallinity of the carbon supports were very highly different, indicating that the polyol method is suitable for fabricating comparable PtRu nanoparticles on different CNM.

Table 4.1. Catalyst loading and average nanoparticle size in the fresh and the used catalyst for macro-DMFC (Pub. I) and micro-DMFC (Pub. II); determined from XRD, HR-TEM images and corresponding histograms.

Catalysts	Macro-DMFC				Micro-DMFC				
	PtRu loading (wt.%)	XRD fresh (nm)	TEM fresh (nm)	TEM used (nm)	PtRu loading (wt.%)	XRD fresh (nm)	TEM fresh (nm)	XRD used (nm)	TEM used (nm)
PtRu-Vulcan	22.6	3.0	3.3	4.5	27.5	4.5	3.6	5.7	5.5
PtRu-GNF	23.5	3.5	3.2	3.5	24.8	3.4	3.6	3.1	3.5
PtRu-FWCNT	26.0	3.3	2.8	3.3	28.3	2.3	2.8	2.1	2.7

Further information on the catalyst size and crystallinity was obtained from XRD (Figure 4.3). The XRD pattern of the fresh catalyst powders showed the diffraction peaks of PtRu alloy crystal faces at 40.2° (111), 46.8° (200), 68.3° (220) and 82.3° (311), characteristic of a face-centered cubic (fcc) structure with a cell constant of 3.88 Å. The average particle size was estimated using Scherrer formula from the Pt(111) peak. The values obtained by XRD are in agreement with the results obtained by HR-TEM images.
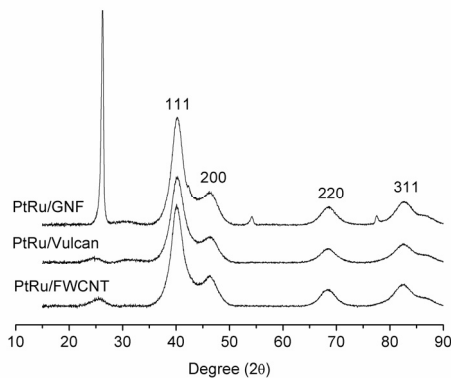

Figure 4.3. XRD patterns of fresh catalyst powders (Pub.I).

The PtRu-catalysts on different carbon supports were evaluated in the 3-electrode cell to determine their electrocatalytic activity for methanol oxidation (Pub.I). Prior to MOR experiments, CO-stripping was done by CO adsorption/oxidation procedure. CO is known to adsorb strongly on the Pt electrode surface, and it can displace most other pre-adsorbed species such as H atoms and anion species from various acidic solutions. This can be used to clean the electrode surface and estimate the electrochemical surface area (ESA). In this work, ESA of the PtRu catalysts on CNM supports were similar, being in the range of 12-14 $m^2 g^{-1}$. This is expected as special effort was done to

synthesize materials with similar particle size and distribution. However, these values have not been used to normalize the currents because details of CO adsorption on Ru surface are unknown; instead the currents were normalized with loading.
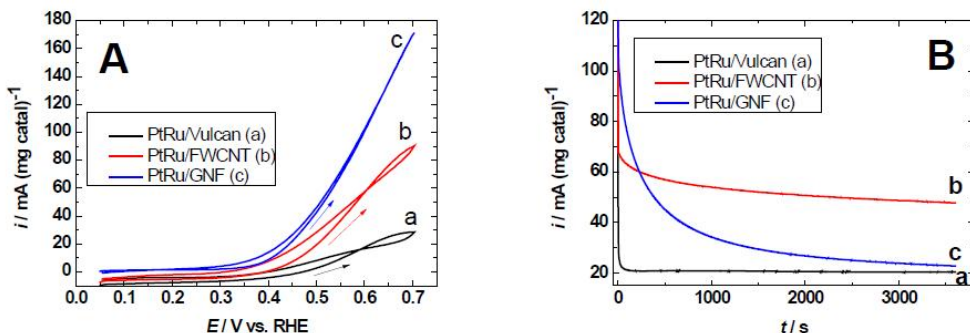

Figure 4.4. MOR on PtRu-catalysts supported on FWCNTs, GNFs and Vulcan;
A) CV at a 10mVs^{-1} scan rate and 1800 rpm, B) CA at 0.7 V for 1 h (Pub.I).

Figure 4.4A shows the activity of PtRu catalysts supported on different carbon supports towards MOR. CVs were carried out in N_2-saturated 1 M methanol solution in 0.1M $HClO_4$ in the potential range from 0 to only 0.7 V, in order to avoid dissolution of Ru from the alloy [57]. It can be seen that both the onset potential and maximum current were improved significantly using the tubular carbon supports. Almost 4-times higher current was obtained with PtRu-FWCNTs and even 8-times higher with PtRu-GNFs compared to PtRu-Vulcan. These results are in accordance with literature reports of 2-fold enhancement with MWCNTs [72, 73] and up to 4-fold increase for GNF-supports [74, 75] with respect to traditional carbon black support. The chronoamperometric results at 0.7 V (Figure 4.3B) indicates that the activity of catalysts decreased over time due to the poisoing of the catalytic sites by MOR intermediates [76, 77]. However, PtRu-FWCNTs showed more stable bahaviour, retaining 69% of the initial current after 1 h, showing better tolerance to methanol oxidation intermediates.

4.4. Fuel cell performance of PtRu-CNMs

The effect of different carbon supports for PtRu catalysts was later investigated in two types of DMFCs with different size and architecture: a macro-DMFC (7.29 cm^2) in Pub.I and a silicon micro-DMFC (1 cm^2) in Pub.II. The evaluation of the catalyst materials in different fuel cell is very useful to understand the effect of fuel cell parameters and components such as temperature, average active area, diffusion layer and flow field design other than only the electrocatalysts.
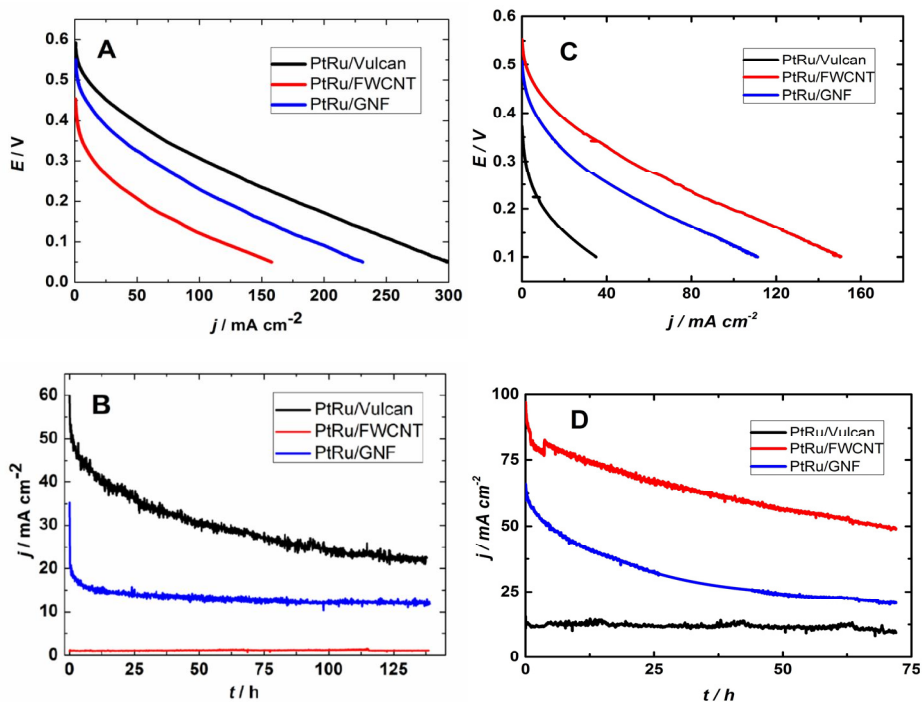
Figure 4.5. Polarization curves and long-term CA measurements of PtRu-CNMs in A,B) Macro-DMFC (Pub.I) at 0.4 V for 6 days (70 °C) and C,D) Micro-DMFC (Pub.II) at 0.2 V for 3 days (30 °C).

The DMFC tests were performed using PtRu-CNMs at the anode with similar catalyst loading (~1 mg cm^{-2}) and a commercial Pt-C catalyst (~2 mg cm^{-2}) at the cathode, all with similar Nafion ionomer content (30 wt.%). Figure 4.5 shows polarization curves and CA measurements for the different catalysts in both macro- and micro-DMFC. In each DMFC, all the conditions are the same except the anode layer structure.

In the macro-DMFC, PtRu-Vulcan electrode produced higher OCV and current density compared to the tubular supports (Figure 4.5A). These results are in contrast to the half-cell measurements (Figure 4.4A). Nevertheles, the performance dcreased over time after 6 days (137 h) of operation (Figure 4.5B). On the other hand PtRu-GNF provided slightly lower initial current density but showed the most stable performance. In the micro-DMFC, PtRu-FWCNTs provided the best OCV and performance in the whole range of current densities, followed by PtRu-GNF and PtRu-Vulcan (Figure 4.5C). In addition, the results of 3-day (72 h) CA meausrements (Figure 4.5D) are in agreement with the trend seen in the polarization curves (Figure 4.5C). Although, micro-DMFC performance with both tubular caron supports decreased over time, the final current density is still cosiderably higher in PtRu-FWCNTs and PtRu-GNFs (by 300% and 130%, respectively) than that of PtRu-Vulcan. On the other hand, the long-term CA measurement in micro-DMFC correlated well with CA behaviour of the catalysts in the 3-electrode cell. As mentioned above, such agreement was not observed in comparison with the macro-DMFC performance. Table 4.2 summarizes the results obtained in both fuel cells.

35

Table 4.2. Performance of PtRu catalysts supported on CNMs in macro- and micro-DMFC.

Catalysts	Macro-DMFC			Micro-DMFC		
	OCV (V)	Max current density (mAcm^{-2})	Instability (in 137 h)	OCV (V)	Max current density (mAcm^{-2})	Instability (in 72 h)
PtRu-Vulcan	0.59	299	14%	0.37	35	11%
PtRu-GNF	0.55	231	1%	0.50	111	32%
PtRu-FWCNT	0.45	158	35%	0.55	151	22%

These results suggest that a coherent understanding of fuel cell performance, requires taking into account many factors such as nanoparticle size alteration, catalyst layer structure and cell architecture. Therefore, a certain catalyst material may not necessarily exhibit the same performance in different fuel cells, because several parameters can affect the catalyst performance when the cell parameters are varied. One reason for the differences encountered in the fuel cells could be the temperature, which has a remarkbale impact on the electrochemical reaction and material transport in the fuel cell. Macro-DMFC measurements were done at 70 °C (common temperature for DMFCs) whereas the micro-DMFC was held at 30 °C close to the room temperature, where the half-cell measurements were performed. At high temeparure of macro-DMFC, mathanol may enter the flowfields and the electrode pores in vaporized form. Consequently, the mass transfer of the reactant and products may greatly differ from the micro-DMFC condition with the liquid mathanol. On the other hand, in order to draw more current in micro-DMFC, the long-term CA measurements were done at lower potential (0.2 V) than in the macro-DMFC (0.4V).

Apart from these factors, alteration of nanoparticle distribution and catalyst layer should be also taken into consideration. The three-phase boundary (TPB), comprising a carbon support with the Pt particles (electron conductor), the ionomer (ion conductor) and the voids (mass transfer), is a key parameter in fuel cell reactions and performance. The pores in the thin film layer can be divided into the primary pores, which exist between catalyst particles (0.02-0.04 µm), and secondary pores, which exist between the agglomerates of catalyst particles and the ionomer (0.04 µm to several µm) [78]. In order to investigate the electrode layer structure, characterization of MEA of the anode materials was done before and after the fuel cell tests.

Figure 4.6 shows SEM micrographs of the cross-section of the anode layers in macro-DMFC before and after the long-term measurement. It can be seen that the fresh anode layer of PtRu-Vulcan was considerably thinner (~8 µm) than that of the tubular carbon supports (~65 µm), even though the same amount of catalyst and ionomer loadings were used for fabrication of all MEAs. In addition, the Vulcan layer structure was expanded almost 3.5 times after 6-day measurements. This structure collapse of the electrode might be one reason for the fast degradation of Vulcan anode layer. In contrast, in micro-DMFC uniform electrode layers with similar thickness (~30 µm) were obtained for all the catalyst materials, due to more experience in MEA preparation using different carbon nanomaterials (Figure 8 in Pub.II). Besides, no severe changes occurred on the secondary structure of the electrodes after long-term stability measurements in micro-DMFC.
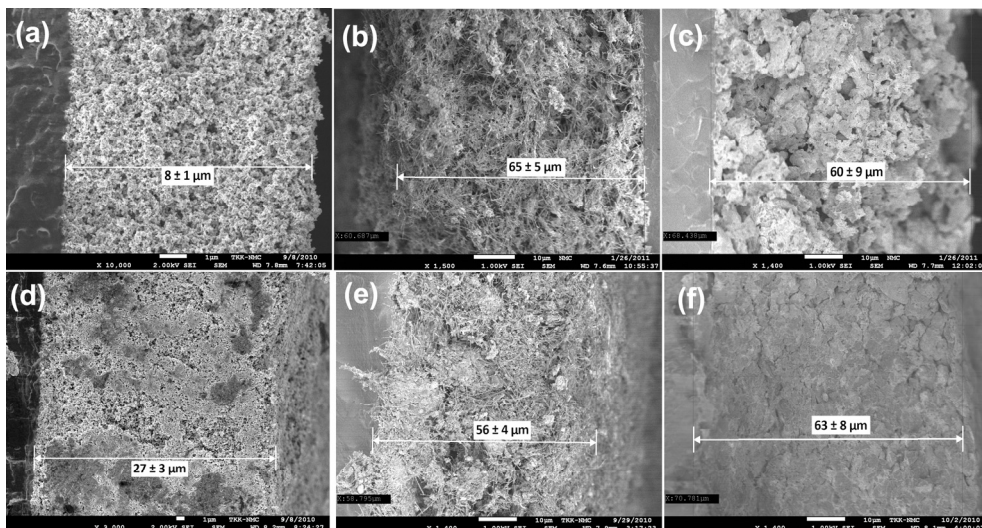
Figure 4.6. SEM images of anode layer cross-sections before (a,b,c) and after (d,e,f) 137 h stability measurements in macro-DMFC; a,d) PtRu-Vulcan, b,e) PtRu-GNFs, c,f) PtRu-FWCNTs (Pub.I).

SEM images in Figure 4.6 also show that the catalyst layers with various carbon supports provide very different secondary structures. Vulcan anode layer exhibits a dense spongy structure with uniform secondary pores, while FWCNT anode layer has little visible porosity with un-even distribution of voids and cracks in the layer. In turn, GNF anode layer has larger macroporous voids compared to the compact structure of FWCNT and Vulcan layers. This open structure could facilitate the flow of reactants and products, explaining the fairly stable performance of the PtRu-GNF electrode in the macro-DMFC. The higher stability encountered for the PtRu-GNF layer motivated further optimization study of the catalyst layer (Pub.III) in order to improve the DMFC performance (section 4.5).

Investigation of the size and distribution of nanoparticles along the electrode structure is also very important to understand the performance degradation. Figure 4.7 shows the catalyst nanoparticles on the carbon supports after fuel cell measurement. The average nanoparticle size after the fuel cell tests are compared with the fresh nanoparticle size in Table 4.1. In both fuel cell types, nanoparticles on Vulcan support aggregated to larger particles to more extent than nanoparticles on the tubular supports. It mainly occurs due to the corrosion of Vulcan support in fuel cell condition [79]. Previously, our in-situ FTIR measurements also verified that the corrosion of carbon black was considerably higher (5-times) than the GNFs in a PEM fuel cell [54]. Besides, Ostwald ripening phenomena may result in clustering of neighboring particles [80] and increase of the particle size distribution in the three electrodes.

In the case of micro-DMFC, a narrower size distribution and smaller average size were observed for the tubular-supported catalysts after the fuel cell tests. It can be postulated that larger nanoparticles were probably detached from the supports, resulted in nanoparticle loss from the TPB and hence activity decrease. The reason might be due to the Si-nanograss diffusion layer in the micro-DMFC, which is only 2 µm long, which cannot efficiently ensure the uniform flow of

37

liquids to the electrode layer. This may result in various local pressure drops inside the electrode leading to nanoparticle detachment from the electrocatalyst. However, carbon cloth diffusion layer with larger thickness can provide enough protection of the catalyst layer, and the even flow of liquids in the electrode layers which is observed in the macro-DMFC.
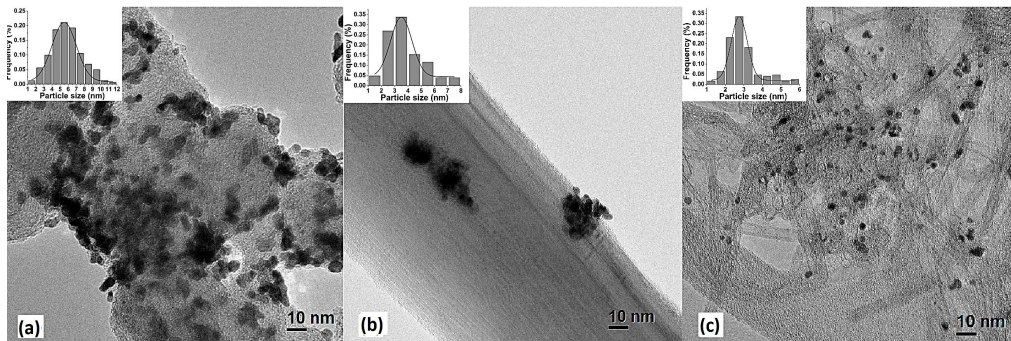

Figure 4.7 TEM images of PtRu catalysts on a) Vulcan, b) GNF and c) FWCNT after micro-DMFC test.

4.5 Optimization of catalyst layer

The interaction between ionomer and catalyst substrate has a significant impact on the catalyst performance due to its influence on the ion conductive phase, the TPB and the total electrode structure. In addition, strong affinity between binder and catalyst materials has shown to prevent catalyst coalescence and detachment [81]. Therefore, when studying different carbon supports in the catalyst layer, the optimum ionomer/carbon ratio for each material should be evaluated in order to obtain the best performance of the fuel cell. The optimum ionomer content depends not only on the carbon support and ionomer type but also on the exact metal to carbon ratio, MEA preparation method, the fuel cell type and operating conditions [82, 83]. For Vulcan-supported catalysts, the optimum Nafion content for the anode layer has been usually reported between 25 wt. % and 40 wt. % [82, 84]. In Publication I and II, all the MEAs were prepared with 30 wt. % Nafion content based on the optimum ratio of the ionomer to carbon black supported catalysts. In Publication III catalysts layers with PtRu-GNFs were prepared by varying Nafion content from 30 to 70 wt. %.
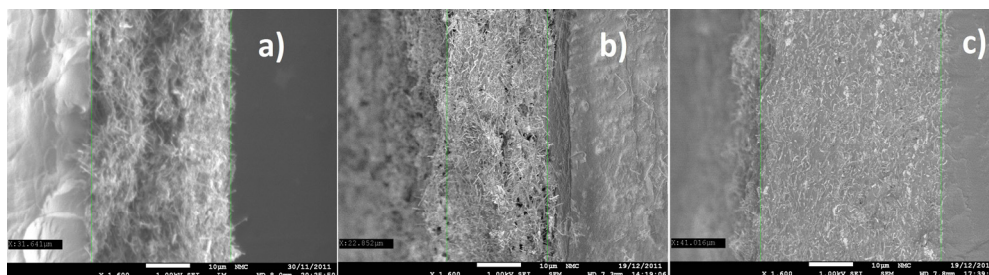

Figure 4.8. PtRu-GNF anode with different Nafion contents a) 30 wt.%, b) 50 wt.% and c) 70 wt.% (Pub.III).

From Figure 4.8 it can be seen that increasing the Nafion content from 30 to 70 wt. % (MEA30 to MEA70) makes the catalyst layer denser and less porous. The specific surface area of the catalyst layers was measured by 1-point BET N_2 adsorption isotherms and confirmed the visual observation from SEM images. BET measurements resulted in 0.8, 07 and 0.3 m^2 g^{-1}, respectively for MEA30, MEA50 and MEA70. The similarity between the BET surface area of MEA70 with that of Nafion membrane (0.3 m^2 g^{-1}) indicates that the catalyst layer in MEA70 resembles the Nafion membrane, while MEA50 and MEA30 exhibited more porous structure.

Figure 4.9 illustrates the significant effect of the ionomer content on the activity and durability of the electrodes in macro-DMFC measurements. With 50 wt. % ionomer content in MEA (MEA50), DMFC performance notably improved. It exhibited the best performance during 9-day (230 h) chronopotentiometric measurements compared to MEA30 and MEA70. This is due to an improved conductivity in MEA50, because both the in-plane and through-plane resistivity reached the minimum value in MEA50 as measured by EIS. That is, the anode catalyst layer with 50 wt. % ionomer turned out to be the best electrode structure, because the voids of the catalyst layer were optimally filled with ionomer to improve the TPB and thus the electroactive surface area. Besides, it influenced the conductivity of the electrode as the optimal ionomer content enable better connection between the GNF supports thus lowering resistivity in the network.
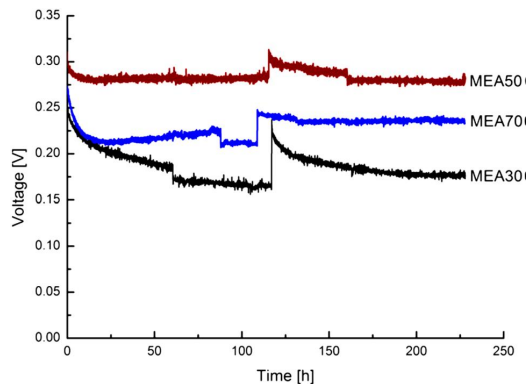

Figure 4.9. 9-day (230 h) CA stability measurements at 27 mAcm^{-2} in macro-DMFC with PtRu-GNF anodes containing 30, 50 and 70 wt% Nafion ionomer content (Pub.III).

5 CNMs as Pt-free catalysts

As mentioned in chapter 2, the ORR is kinetically sluggish as it is a complicated multi-electron transfer process, and only precious metals can effectively catalyze the reaction. In 1964, Jasinski for the first time reported the use of non-noble catalysts for ORR, and studied the activity of cobalt phthalocyanine in a fuel cell cathode catalyst [85]. After that, variety of nitrogen-coordinated transition metal macromolecules (metal-N_4-macrocycles) were explored for ORR catalysis [86, 87]. These complexes were attractive because of their lower cost compared to noble metals and their higher tolerance to methanol oxidation, especially for DMFC applications. Their catalytic activities could be also modulated by changing the structure of the macrocyclic compound [88]. However, the major drawback of these catalysts was their low stability in acidic media, as a result of a loss of their active sites, due to the attack of hydrogen peroxide generated during ORR [89]. Later on, it was discovered that the heat-treatment of carbon-supported M-N_4 macrocycles in an inert atmosphere could improve their stability and catalytic activity [88, 89]. Afterwards, Gupta et al. reported a novel synthesis method (using non M-N_4 macrocycles) that consisted on mixing a nitrogen-containing polymer, transition metal salts and high-area carbon, followed by a thermal treatment process [90]. Since then, numerous reports were published on the use of cheaper and more common inorganic salts, with variety of N-containing compounds and carbon materials as starting materials [91]. It was also shown that the nature of the metal in the precursor and the metal loading played a crucial role on the catalytic activity of the resulting material [86, 92, 93]. On the other hand, nitrogen is a necessary component in order to form the catalytic active sites. The type of nitrogen source has a large effect on the resulting activity [94].

Among all the relevant parameters, the starting carbon materials also play key role in obtaining high ORR activity. Especially, with the emergence of novel carbon nanomaterials with superior properties, the research on metal-free catalysts has become very promising. The introduction of heteroatoms into the hexagonal carbon lattice can modulate the chemical and electrochemical activities due to the alteration of electronic structure [95]. In particular, nitrogen is considered as an excellent dopant for carbon materials due to its comparable atomic size and its five valence electrons to form strong valence bonds with carbon atoms. In this context, N-doped carbon nanomaterials (N-CNMs), with an extra electron supplied by the nitrogen atom, exhibit higher electron density and a raised highest occupied molecular orbital (HOMO) energy level of sp^2 carbons [12]. Moreover, addition of nitrogen varies the charge distribution of the carbon network so that the C atoms adjacent to N become more positively charged, resulting in an enhanced interaction with the adsorbing molecule and thus lower activation barrier for its decomposition [96].

Recently, a variety of metal-free nitrogen doped CNMs have been synthesized in the form of CNTs [97-102], CNFs [103, 104], graphene [105, 106], mesoporous carbon [107], carbon nanocages [108], carbon spheres, hollow carbon nanoparticles [109], etc. In this thesis the synthesis and electrocatalytic activity of N-FWCNTs and N-GNPs for the ORR have been investigated.

5.1 Preparation of N-CNTs

N-CNTs can be produced by "in-situ" or "post-treatment" doping methods. In-situ doping methods incorporate nitrogen atoms into the carbon network simultaneously as CNTs grows. Chemical vapor deposition (CVD) is a well-known method requiring the aid of a metal catalyst (Fe, Co, Ni compounds), and in compatible with different types of carbon precursors and nitrogen-containing reagents. Nitrogen precursors can be supplied as gas mixtures such as CO/NH_3 [98], liquid organic precursors like pyridine [100], acetonitrile [99] or nitrogen containing polymers [110].

Through the mechanistic study of ORR, Wiggins-Camacho and Stevenson reported that the metal residues originating from a typical metal-catalyzed synthesis contribute to the ORR catalysis [111]. Any metal residues can also disturb the characterization and lead to misidentification of the effect of nitrogen catalytic sites. Moreover, any acid leaching to remove metal residues can easily damage the nitrogen functionalities due to their relatively high reactivity. In this regard, Wang et al. synthesized N-CNTs by detonation-assisted CVD using melamine without any metal catalysts [102]. However, the resulted bamboo-like N-CNTs did not show good ORR activity, despite of very high nitrogen content (~20 at.%). Arc discharge method using a melamine/graphite rod was also reported as an alternative in-situ doping approach (without the need for metal catalysts) but this method yields small scale production [112].

A high catalytic activity in heterogeneous reactions is expected to come from the accessibility and exposure of active sites to the reactant molecules. In in-situ doping methods, usually N atoms are incorporated inside the inner CNT walls, so they are not accessible for the oxygen molecules. For example, in the case of bamboo-like N-CNT structures, N atoms were concentrated at the inner curved joints of the compartments and trapped between the graphitic walls [113]. In some cases, nitrogen gas is trapped in the inner compartments which hinders the conductivity of N-CNT and not rendering any catalytic activity [114]. In this regard, an efficient N-CNT should be obtained by incorporating accessible N-atoms at the surface while preserving the inner CNT structure for an efficient electron transfer and conductivity. In the post-treatment doping techniques, purified CNTs are treated with different nitrogen precursors such as NH_3 [115], urea [116], dicyandiamide [117] or polymers including polyaniline (PANI) [55] and polypyrrole [104], then followed by a thermal annealing at high temperatures to form graphitized N-doped layer around the intact CNT walls.

Among nitrogen precursors used for post-treatment doping, PANI has received considerable attention. It is a conducting polymer with low price, good processability, stable and controllable conductivity over a wide potential range [118-120]. Its electrical conductivity is strongly influenced by the synthetic method and conditions. The room temperature electrical conductivity of PANI can reach maximum values around 100 S cm^{-1}[121]. Moreover, PANI can strongly interact

with CNT walls due to the π-π conjugation of quinoid rings of PANI and the benzenoid rings of CNTs [122].

In this thesis, we used FWCNTs as starting carbon material for the post-treatment doping method, which is rarely reported in the literature. Nitrogen doping of SWCNTs (with only a single layer), dramatically decreases the conductivity, and in turn impacts the catalytic activity. On the other hand, MWCNTs with large diameter contains a lot of inactive inner layers which are not contributing to the reaction. Using FWCNTs with intermediate conductivity and structural perfection (between SWNCTs and MWCNTs) minimizes the volume and mass of inactive parts, meaning that higher heterocatalytic activity per mass of catalyst can be obtained.

FWCNTs were first treated with aniline to obtain a core-shell FWCNT-PANI composite [123] then followed by annealing at high temperatures. The synthesis method of N-FWCNT is illustrated in Figure 5.1 and described in detail in Publication IV. Shortly, the thin PANI layer was obtained by chemical oxidative polymerization of the aniline monomer using ammonium persulfate (APS). Part of the FWCNTs was subjected to oxidative functionalization (described in section 4.1) before coating with PANI, to investigate the effect of surface oxygen functional groups in the final doping. The resulting PANI-FWCNTs were pyrolyzed for 1 h at 600 °C or 900 °C to obtain N-FWCNTs. The FWCNT samples are coded as: FW-Pr for the merely purified "pristine" FWCNTs, FW-F for the oxidatively functionalized FWCNTs, NFW-Pr-900 for the N-FWCNTs pyrolyzed at 900 °C using purified FWCNTs, NFW-F-600 and NFWF-900 for the N-FWCNTs where PANI was pyrolyzed at 600 °C and 900 °C respectively, on the functionalized FWCNTs.
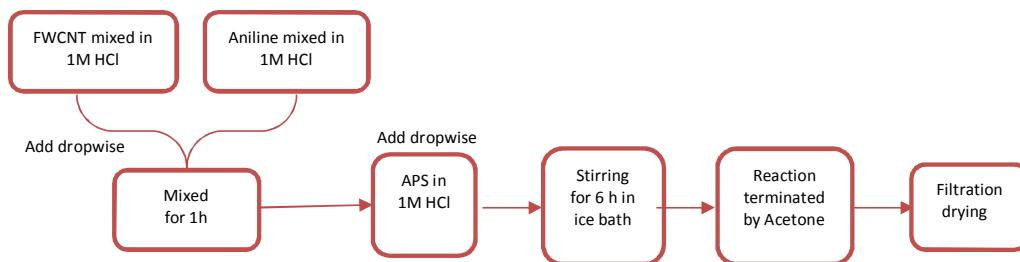

Figure 5.1. Schematics of chemical oxidative polymerization of aniline on FWCNTs.

5.2 Characterizaion of N-FWCNTs

Surface morphologies of pristine FWCNTs, PANI-FWCNTs and the final pyrolyzed N-FWCNTs are shown in Figure 5.2. It can be seen that the PANI layer is wrapped around the nanotube in the PANI-FWCNT composite (Figure 5.2 b). PANI is known to be positively charged in acidic media and thus is attracted electrostatically to the negatively charged oxygen functional groups in FWCNTs, favoring PANI coating on CNTs rather than the formation of bulk polymer [55]. After the pyrolysis a thin wrinkled N-doped layer is left at the outer wall of FWCNT (Figure 5.2 c).
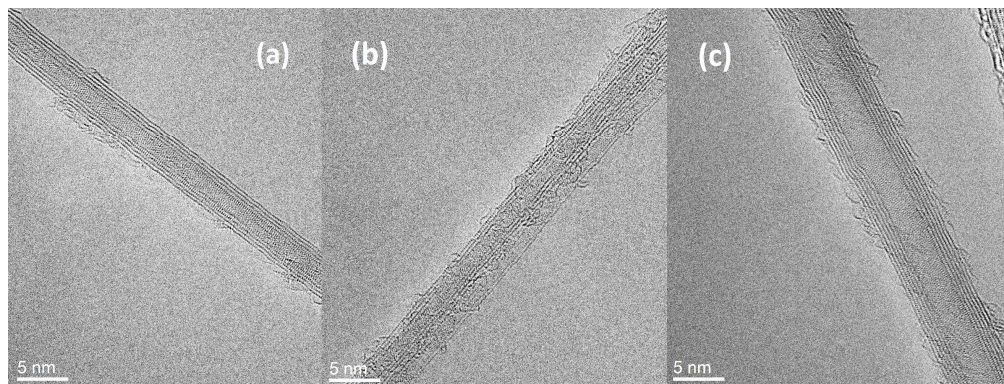
Figure 5.2. TEM images of a) FWCNTs, b) PANI-FWCNTs and c) N-FWCNTs (Pub. IV).

Raman spectra for the pristine and treated FWCNT samples were also done (Figure 2 in Pub. IV), and clearly indicated the presence of conduction PANI (emeraldine form) in the PANI-FWCNT composites. Table 5.1 shows the D/G band intensity ratio obtained for the pyrolyzed samples. It can be seen that the pyrolysis temperature had a notable effect on the graphitization degree of the N-doped layer so that at 900 °C a lower D/G ratio was obtained, meaning that the samples at 900 °C reached to a higher graphitization degree than the one at 600 °C.

The data obtained from XPS spectra (Figure 3 in Pub.IV) are presented in Table 5.1, indicating that the total nitrogen content in all the N-FWCNT samples is only below 1 at.%. In addition, while the pyrolysis temperature increased, the nitrogen content was decreased due to the loss of nitrogen-containing gases [124]. However, for a same pyrolysis temperature (900 °C) a higher nitrogen content was obtained with the functionalized sample due to the stranger interaction of PANI with the oxygen functional groups [55].

Table 5.1. Data obtained from Raman and XPS spectra of pristine FWCNTs and different N-FWCNTs.

	FW-Pr	*FW-F*	*NFW-F-600*	*NFW-F-900*	*NFW-Pr-900*
I_D/I_G	0.31	0.37	0.48	0.22	0.24
O at.%	1.2	3.7	0.8	0.87	0.36
N at.%	--	--	0.72	0.56	0.27
pyridinic-N (%)	--	--	28	35	31
pyrrolic-N (%)	--	--	44	8	8
graphitic-N (%)	--	--	20	44	46
pyridine-N-oxide (%)	--	--	8	13	15

The local structure and bonding type of N atoms in the graphitic network has strong influence on the charge density and chemical states of nitrogen sites. Four types of N-bonding configurations were identified by deconvolution of the N1s peak of the XPS spectra and schematically depicted in Figure 5.3. Pyridinic-N (at ca. 398.3 eV) refers to N atoms at the edges, bonded to two carbon atoms donating one p-electron to the π-system. Pyrrolic-N atoms bond to two carbon atoms in a 5-membered ring and contribute two p-electrons to the π-system, hence they have higher binding energy (at ca. 400.1 eV). Graphitic-N (or quaternary-N) atom (at ca. 400.9 eV) substitutes a carbon atom and bonds to three neighbouring carbon atoms. Pyridinic N-oxide bonds to two carbon atoms and one oxygen, clearly distinguished with a binding energy shift of +5 eV (at ca. 403.5 eV)

43

compared to pyridinic-N [125]. The distribution of the different N-bonding configurations in each sample is presented in Table 5.1 and will be discussed in connection with the ORR activity in the next section.
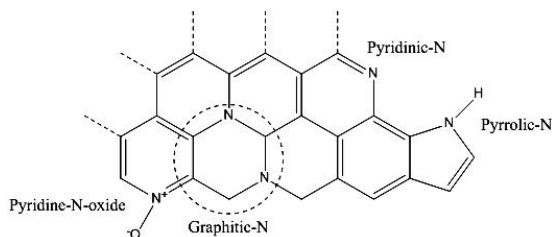

Figure 5.3. Nitrogen-bonding configurations in a graphitic sheet.

5.3 ORR activity of N-FWCNTs

The electrocatalytic activity of N-FWCNTs was evaluated using CV and RDE methods (Figure 5.4) in a three-electrode cell in alkaline media (0.1 M KOH). It can be seen that the 2-step ORR process on pristine FWCNT has been significantly improved to 1-step on N-FWCNT (Figure 5.4 a). With increasing annealing temperature from 600 °C to 900 °C, the electrocatalytic activity was enhanced as indicated by the higher current density, more positive onset and peak potentials (Table 5.2). It can be due to the higher graphitization degree of the N-doped layer (lower D/G ratio) and larger contribution of graphitic-N and pyridinic-N sites (from XPS data), which promote the electron transfer and cause a positive shift of the reduction potential [126].
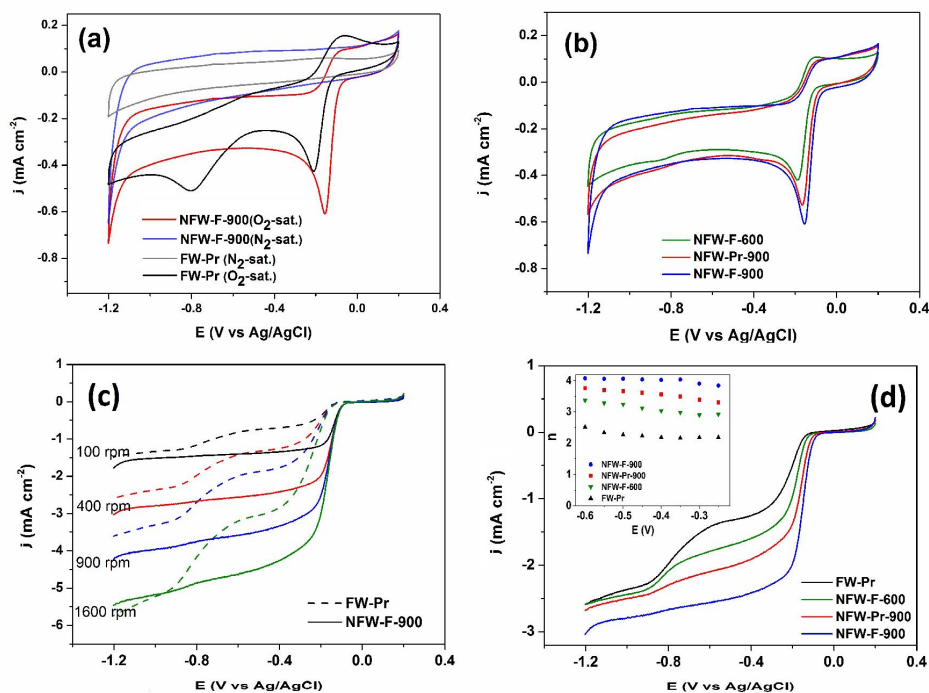

Figure 5.4. Electrochemical characterization of ORR at N-FWCNTs compared to pristine FWCNTs: a,b) CV at 10 mV/s and c,d) RDE measurements at 5 mV/s in 0.1 M KOH (Pub. IV).

The enhanced electrocatalytic activity of N-FWCNTs was quantitatively evidenced by RDE experiments (Figure 5.4 c&d) and the electron transfer number calculated from the K-L equation. The average *n* value in the potential range from -0.3 to -0.5 V followed the increasing trend: FW-Pr (2.1) < NFW-F-600 (3.1) < NFW-Pr-900 (3.5) < NFW-F-900 (4.0). It can be seen that oxygen functionalization of FWCNTs has siginificant effect on ORR electrocatalytic activity of the resulting N-FWCNT.

Table 5.2. Onset and peak potentials for the ORR obtained from CV" and RDE* measurements, and kinetic parameters calculated from the Tafel plots (Figure 5.5b).

	Purified	*NFW-F-600*	*NFW-F-900*	*NFW-Pr-900*	*Pt-C*
Onset potential (V)*	-0.07	-0.06	-0.03	-0.04	0.05
Peak potential (V)"	-0.2	-0.18	-0.15	-0.16	-0.15
k (10^{-3} cm s^{-1})	--	0.4	2.8	1.6	3.1
j_d (µA)	--	3.1	21.2	11.9	23.3
α	--	0.2	0.42	0.36	0.49

N-CNTs have been recently reported to be an efficient catalyst for decomposition of H_2S to solid sulfur [127] as well as oxidative dehydrogenation of aromatic and alkenes [128]. Our N-FWCNT samples also showed activity for the hydrogen evolution reaction (HER). Figure 5.5a shows that bubbles are formed at a GC electrode modified with NFW-F-900 while sweeping the potential to around -1.2 V. It can be suggested that the active sites involved in the ORR can also catalyze the HER at more negative potentials. It is revealed by the emergence of a large peak at around -1.2 V in cyclic voltammograms (Figure 5.4a). The occurrence of oxygen evolution at N-CNTs was recently observed elsewhere [129].
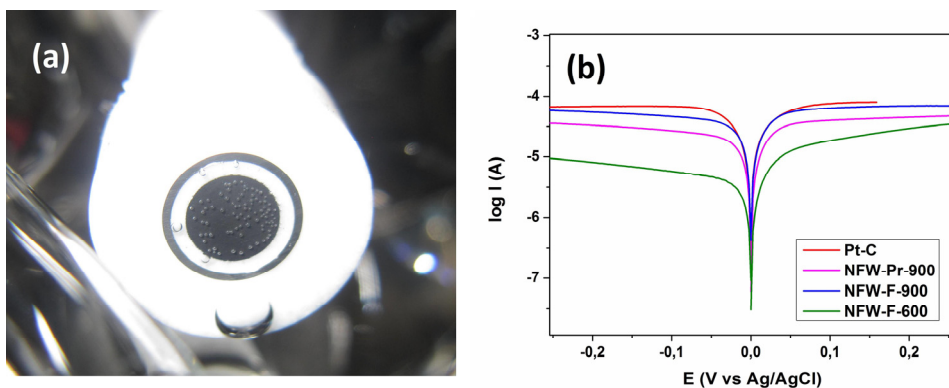

Figure 5.5. a) HER at a GC-modified with NFW-F-900 in N_2-sat. 0.1M KOH at 5 mV/s, b) Tafel plots after injection of H_2O_2 (0.4 mM) in N_2-sat. 0.1M KOH at 0.17 mV/s and 1500 rpm (Pub. IV).

We further characterized ORR electrocatalytic activity by RRDE measurements in comparison with a commercial Pt-C. Figure 5.6 shows that ORR electrocatalytic activity of FWCNTs was remarkably improved after N-doping treatment, with a significantly lower amount of hydrogen peroxide and much higher electron transfer number very close to Pt-C electrode.

To study the electrokinetics of H_2O_2 on the modified electrodes, a given volume of H_2O_2 was pipetted into the deaerated electrolyte and the potential was swept in the 0.4 ± 0.25 V regions in the

RDE system. The calculations from Tafel plots (Figure 5.5b and Table 5.2) confirmed the faster kinetics of H_2O_2 electroreduction on NFW-F-900 (close to that of commercial Pt-C catalyst). The kinetic rate constants obtained for H_2O_2 decomposition follow the same trend as ORR activity: FW-Pr < NFW-F-600 < NFW-Pr-900 < NFW-F-900 < Pt-C. Specially, NFW-F-900 with k= 2.8 × 10^{-3} cm s^{-1} performed very similarly to Pt-C electrode (3.1 × 10^{-3} cm s^{-1}), supporting the RRDE measurements. The high electrocatalytic activity of N-FWCNTs toward electroreduction of hydrogen peroxide makes this materials useful even for biosensing applications where low amount of H_2O_2 needs to be detected as by-product of a biomolecule decomposition [130].
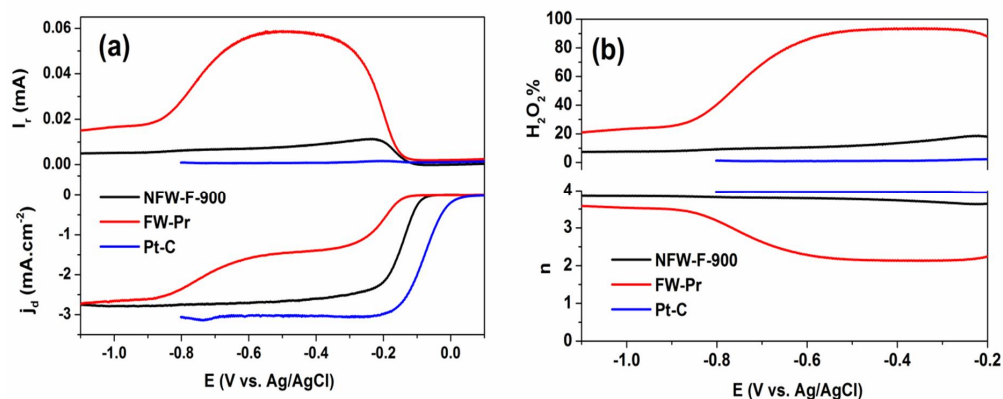

Figure 5.6. RRDE measurements: a) disk and Pt-ring current densities, b) H_2O_2% production and number of transferred electrons in O_2-sat. 0.1 M KOH at 5 mV/s and 400 rpm (Pub. IV).

NFW-F-900 showed remarkable ORR electrocatalytic activity even though the nitrogen content (0.57 at.%) was much lower compared to previously reported values in literature (Table 3 in pub.IV) that usually refer to nitrogen levels higher than 3 at. % [97, 110, 113, 131]. The differences in activity may arise from the N-doped layer at the outer nanotube walls, which formed an open porous structure with abundant edge planes. The efficient utilization of the highly accessible nitrogen atoms that are integrated in the N-doped layer on the FWCNT surface, together with the intact inner walls, render N-FWCNTs with high electrochemical activity. The significance of the accessible surface nitrogen atoms on the ORR electrocatalytic activity of N-CNTs has been recently highlighted by Tian et al [129].

The reason behind the enhanced activity of N-CNTs is still under debate, attracting numerous experimental and computational research to identify the nature of the catalytic sites. Some reports correlated the ORR activity to the increase of nitrogen content [100, 131], while other ones claimed that ORR acitivity was not improved by nitrogen content [115, 132]. If the nature, structure and reaction mechanism of the catalytic sites is well undrestood, new experimental procedures can be designed in order to develop more efficient catalysts for fuel cell applications. However, there is still large controversy on which type of nitrogen functionalities are the active sites for ORR. Several studies have demostrated the superior activity of pyridinic-N on promoting ORR

electrocatalyctic activity [110, 113, 116]. In contrast, other studies reported that N-CNTs containing larger amount of graphitic-N functionalities exhibited higher ORR activity [55, 115].

In order to shed more light on this issue, we further inverstigated the influence of the type of nitrogen sites on the ORR electrocatalytic activity by trasforming N-functionalities via increasing pyrolysis temperature. Here, PANI-FWCNTs were produced (on functionalized FWCNTs) and then pyrolyzed for 2 h in argon flow at 600, 750 and 900 °C. Figure 5.7 shows that by increasing temperature from 600 to 900 °C the total nitrogen content decreased to almost half, but the ORR electron transfer number was greatly enhanced. Moreover, the distribution of nitrogen functionalities was changed. Graphitic-N (quaternary-N) content was rapidly increased with temperature while pyrrolic-N content was significantly reduced. Pyridic-N and pyridinic-N-oxides did not show a major change.
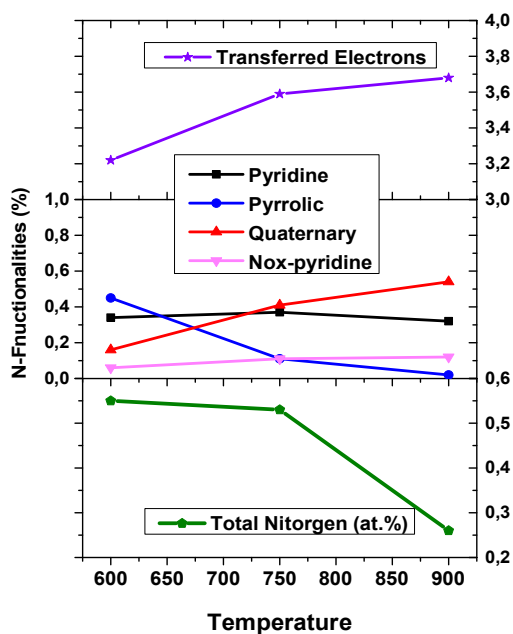
Figure 5.7. Effect of pyrolysis temperature on total nitrogen content, relative content of N-functionalities and ORR electron transfer number (unpublished).

These results are in agreement with the reported literature that pyrrolic-N sites transform to pyridinic-N at moderated temperatures (400-600 °C) via a dynamic surface arrangement. Further, at higher temperatures (T > 600 °C) pyridinic-N sites transform into graphitic-N through a ring condensation mechanism, indicating that graphitic-N is the most thermally stable structure [55, 124, 126]. The thermal transformation of nitrogen functionalities for PANI treated samples is schematically shown in Figure 5.8.

Figure 5.8. Schematics of transformation of N-functionalities driven by annealing effect (unpublished).
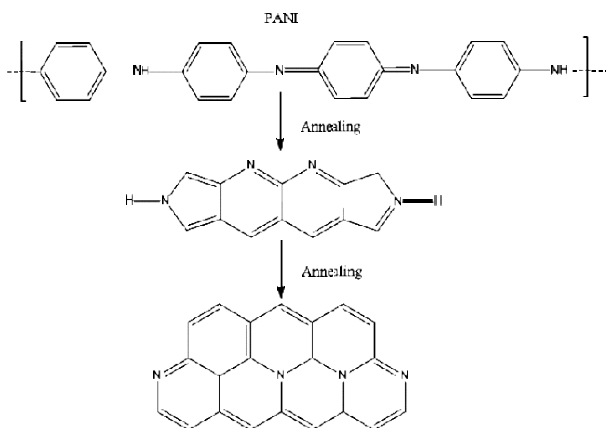
To further investigate the effect of the type of N-functionality, samples with similar nitrogen content were compared. These samples were obtained by varying the synthesis parameters (acid treatment time, PANI amount and pyrolysis time). The obtained results were very interesting. As shown in Figure 5.9 and Table 5.3, the limiting currents are slightly lower in the samples with higher graphitic-N content, and more hydrogen peroxide was produced. It seems that pyridinic-N may also play role in hydrogen peroxide decomposition in the ORR process. Li et al. previousely [133] suggested that the graphitic-N can influence the limiting current density, whereas pyridinic-N may improve the onset potential and favour the reaction mechanism from a predominantely $2e^-$ process to a $4e^-$ pathway. In another study, Yasuda et al. were selectively synthesized N-graphene with abindant pyridinic-N or graphitic-N sites using different N-containing precursors. They reported that that graphitic-N species favour a $2e^-$ pathway, whereas pyridinic-N species induce a $4e^-$ reduction pathway [134].

Table 5.3. Comparison of nitrogen functionalities and electron transfer number for N-FWCNTs prepared with different synthesis parameters.

Sample	Total N	Pyridinic-N	Pyrrolic-N	Graphitic-N	Pyridinic-NOx
NFW-F-900	0.56	35	8	44	13
NFW-F-900(2h)*	0.26	32	2	54	12
NFW-F-900(50p-6h)"	0.57	29	0	60	11

* the same acid treatment time and PANI amount as NFW-F-900 but 2h pyrolysis time.

" longer acid treatment (6h), more PANI (50 wt. %) and longer pyrolysis time (2h) than NFW-F-900.
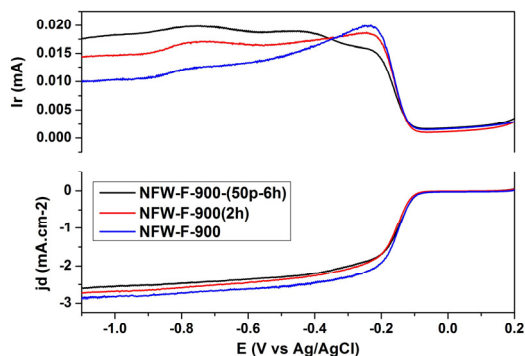
Figure 5.9. Disk and Pt-ring current densities from RRDE measurments: N-FWCNTs with different N-functionalities in O_2-sat. 0.1 M KOH, at 5 mV/s and 400 rpm (unpublished).

Finally, the effect of catalyst loading on the reaction mechanism was studied. Figure 5.10a shows that a decrease in the catalyst loading resulted in lower limiting current densities and higher H_2O_2 fractions. In addition, the onset potential was shifted to more negative potentials with lower catalyst loading. The effect of electrode rotation rate was also studied at constant loading. Figure 5.10b shows that at higher rotation rates the H_2O_2 fraction was larger. Bonakdarpour et al. also observed similar impact of catalyst loading on the ORR activity in RRDE experiments, when varying the Fe/N/C catalyst loading in acidic media [135]. These observations were further predicted in by computational modeling by Jaouen et al [136].
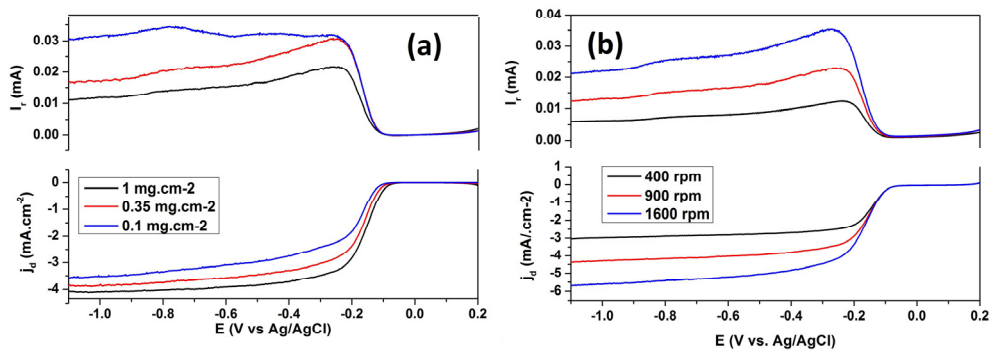
Figure 5.10. RRDE experients with N-FWCNTs in O_2-sat. 0.1 M KOH; a) effect of catalyst loading and b) effect of rotation rate on disk and Pr-ring currents (unpublished).

Simplified mechanisms for the ORR was previously shown in Figure 2.5. Generated H_2O_2 molecules are able to react on the catalytic sites either electrochemically to produce water or chemically to decompose into oxygen and water (with no exchange of electrons). Then the oxygen molecule generated from the disproportionation reation may be again electrochemically reduced into hydrogen peroxide. Several such cycles on a large number of O_2 molecules could result in an apparent near $4e^-$ reduction of O_2 even if the electroreduction of H_2O_2 to H_2O never occurs [137].

Therefore, both processes may convert all the produced H_2O_2 molecules to water in the bulk of the electrode, resulting in an apparent close to 4e$^-$ reduction pathway for the ORR.

It is worth to menthion that modifying a glassy carbon electrode with CNT aggregates results in a porous electrode. It means that lowering the electrocatalyst loading is equal to reducing the porous electrode thickness. When the electrode is thick (high loading) H_2O_2 molecules which are produced within the porous electrode at a given active site must first diffuse across the porous electrode before reaching the electrolyte. On the other hand, rotation rate works as a driving force to push H_2O_2 molecules diffusing out of the electrode. Therefore, in a porous electrode, H_2O_2 molecule produced at *one* site has a high probability to be electroreduced or disproportionated at *another* site before it may reach to the electrolyte. In a smooth electrode, it is probability much lower and the electroreduction might occur at one site. [136].

Threfore according to above results, we propose a *pseudo-4e$^-$* model for the ORR process on N-FWCNTs in alkaline media. Figure 5.11 showes that first a dissociative adsorption of O_2 molecules occurs on graphitic-N sites, then the produced hydroperoxide further decomposes chemically or electrochemically on pyridinic-N sites. In contrast, on Pt-C catalyst no influence of catalyst loading and rotation rate on the H_2O_2 fraction was observed in our experiments (data not shown), which is a proof of a direct 4e$^-$ ORR mechanism. Further characterization should be done to corroborate the proposed mechanism, which can be the topic for future research.
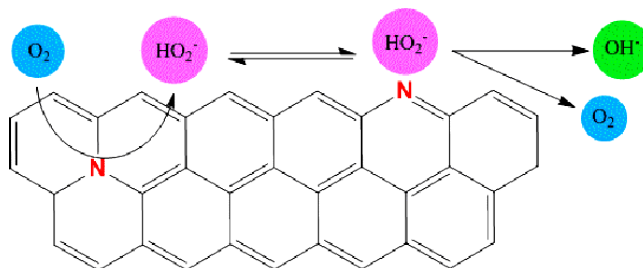
Figure 5.11. Proposed model for the ORR process on N-FWCNTs (unpublished).

5.4 Fuel cell measurements with N-FWCNTs

Finally, the performance of N-FWCNTs was evaluated in the cathode of an alkaline direct methanol fuel cell. Figure 5.12 compares the polarization curves and power density for NFW-F-900 and commercial Pt-C catalysts in the cathode of an alkaline DMFC. NFW-F-900 outperforms the Pt-C catalyst at low and medium current densities, and then gradually reaches almost identical performance in the high current density region. The OCV obtained with NFW-F-900 (0.5 V) is significantly higher than with Pt-C (0.44V) due to a higher resistance to methanol crossover. NFW-F-900 provided a maximum power density of 0.75 mW cm^{-2} which is higher than that of the Pt-C catalyst (0.70 mW cm^{-2}). In addition, our further fuel cell characterization showed that when the

more practical oxidant (air flow) was used at the cathode, N-FWCNTs exhibited significantly superiour performance (0.73 mW cm^{-2}) compared to the Pt-C catalyst (0.18 mW cm^{-2}) [138].
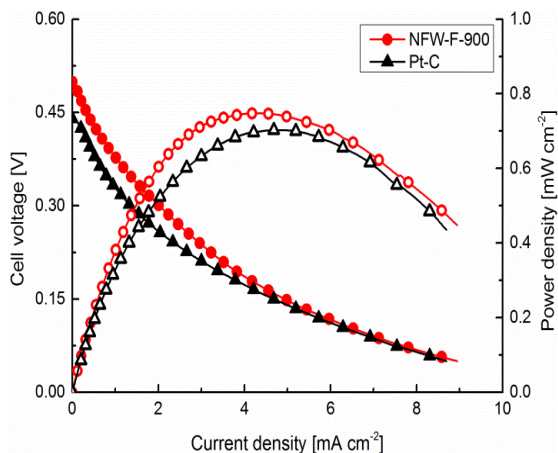

Figure 5.12. Polarization curves and power densities of NFW-F-900 and Pt-C catalysts at the cathode of an alkaline DMFC (Pub. IV).

5.5 Nitrogen doping of graphene materials

Extensive research has recently targeted graphene applications because it has outstanding properties and can be produced at lower cost than CNTs. As with CNTs, chemical doping is an effective approach to tailor the properties of graphene, which can greatly broaden its applications. There are two main ways to dope graphene: i) the adsorption of gas [139], metal [140], or organic molecules [141] on the surface of graphene, and ii) substitutional doping, which introduces heteroatoms such as nitrogen and boron into the carbon lattice [142].

Substitutional N-doping of graphene can be done by two approaches, in similar way as with N-CNTs: in-situ and post-treatment methods. The in-situ approach includes several methods such as CVD, segregation growth, solvothermal and arc-discharge. CVD, as a widely used method, consists in flowing gas mixtures (NH_3, CH_4 or C_2H_4) or liquid organic precursors (acetonitrile, pyridine) over catalyst substrates such as Cu or Ni at high temperatures [143]. By varying the flow rate and the ratio of carbon to nitrogen source, the nitrogen content of N-graphene can be controlled. The number of layers can be also adjusted by the flowing time of the precursors. The type and relative content of N-functionalities are influenced by the type of precursors, ratios, catalyst and the growth temperature. In the segregation approach, sequential layers of N-containing boron and C-containing Ni are deposited on SiO_2/Si substrate by electron beam evaporation and annealed in vacuum. In this method, C atoms segregate out onto the Ni surface and combine with N to form N-graphene while boron atoms are trapped by Ni [144]. In the arc-discharge method, a carbon source electrode (usually graphite) is evaporated in the presence of NH_3 or pyridine vapor at high temperature [142]. The solvothermal approach consists of mixing Li_3N and CCl_4 at mild temperatures around 300 °C for the synthesis of N-graphene [145].

Post-treatment doping methods include thermal annealing, plasma treatment and treatment with hydrazine. In the thermal annealing approach, graphene or graphene oxide (GO) are treated with various nitrogen precursors such as NH_3, melamine, urea or dicyandiamide and then annealed at high temperatures (500-1000 °C). In the plasma treatment, graphene or GO are placed in NH_3 or N_2 plasma so that carbon atoms can be partly replaced by N [146, 147]. Finally, N-graphene can also be obtained by reducing GO with hydrazine at low temperatures (< 120 °C) using NH_3 as precursor [106]. Most of these doping techniques are costly, complicated and apply highly toxic or volatile nitrogen substances, hence the development of simpler, environmentally friendly and scalable methods is highly necessary.

Recently, interesting methods have been proposed for the large scale and low-cost production of graphene by graphite exfoliation using ionic liquids (ILs) by means of mechanical grinding and/or electrochemical techniques [148, 149]. These novel methods allow production of pristine graphene sheets from direct exfoliation of graphite rather than producing GO which then have to be reduced [150]. The combination of the unique properties of ILs and graphene will help to speed up the uptake of graphene materials in currently explored applications and possibly in new areas. ILs are salts with melting point below 100 °C and good thermal stability. Their very low vapor pressure and non-flamability in contrast to the volatile organic solvents make them environmentally friendly alternatives. Most importantly, ILs have surface tensions closely matching the surface energy of graphite, which is a key prerequisite of solvents for direct exfoliation of graphite [96, 148]. Recently, N-graphene sheets with high N/C ratios were obtained by electrolysis of graphite electrode in N-containing electrolyte, followed by pyrolysis at 400 °C [151].

5.6 Preparation and characterization of N-GNPs

In this study, we have explored different imidazole/imidazolium derivatives for the nitrogen doping of GNPs by a facile and low-cost post-treatment approach. The morphology and specification of GNPs were described in section 3.1. Figure 5.13 shows the nitrogen-containing precursors used, with different nature and charge: $BMIBF_4$ (IL), PVI (neutral polymer) and PBVIBr (poly (ionic liquid), PIL). PILs are polymerized ionic liquids, which combine some of the unique properties of ILs with the common profile of polymers. They also contain cationic and/or anionic moieties with nitrogen atoms in each repeating unit.

$BMIBF_4$
1-Butyl-3-methylimidazolium tetrafluoroborate

PVI
Poly(vinylimidazole)

PBVIBr
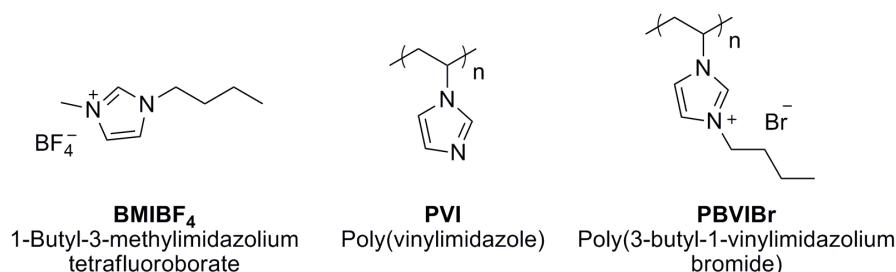Poly(3-butyl-1-vinylimidazolium bromide)

Figure 5.13. Nitrogen precursors used for GNP functionalization and N-doping (Pub.V).

GNPs were first functionalized with the nitrogen precursors by co-dispersing and stirring for long time of 15 h (Pub. V). Later, nitrogen-doped GNPs (N-GNPs) were obtained by pyrolysis of the corresponding functionalized GNPs (f-GNPs) at 900 °C for 1h. N-GNP samples were abbreviated as N-GNP1, N-GNP2 and N-GNP3, for those obtained from BMIBF$_4$, PVI and PBVIBr, respectively.

The surface functionalization of GNPs was confirmed by thermal gravimetric analysis (TGA) and the amount of nitrogen precursors in f-GNPs was determined (Figure 2 in Pub.V). It was found that the N-precursor amount in f-GNPs followed the order: BMIBF$_4$ (20.0 wt. %) > PBVIBr (15.0 wt. %) > PVI (13.3 wt. %). It seems that the charged properties of ILs resulted in higher functionalization degree due to the stronger electrostatic and π-π interactions. In order to determine gravimetrically the nitrogen content in each f-GNP, estimation was done by considering the amount of precursors (TGA data) and the relative N content in the precursor. The N content (wt.%) in f-GNPs decreased in the following order: 4.0 (PVI-GNP) > 2.5 (BMIBF$_4$-GNP) > 1.8 (PBVIBr-GNP). This trend correlates with the surface N content (at.%) obtained by XPS analysis (Figure 3 in Pub.V) for N-GNPs: 3.3 (N-GNP2 from PVI) > 1.9 (N-GNP1 from BMIBF$_4$) > 1.6 (N-GNP3 from PBVIBr).

The relative content of each N-functionalities are summarized in Table 5.4. Notably, despite the different nature of the nitrogen precursor, the relative distribution of N-functionalities is similar, with a dominant content of graphitic-N (quaternary-N) sites (48-50%) followed by pyridinic-N (35-38%) and pyridinic N-oxides (12-15%). However, there was no signature of pyrrolic-N sites within the error bars of the fit. The similar distribution of N-functionalities in all N-GNP samples could be due to the same conditions at which f-GNP samples were pyrolyzed. Stanczyk et al. reported that after calcination of precursors with different nature at 800 °C, similar N-functionalities were obtained [124]. The influence of annealing temperature on configuration of N-functionalities has been discussed in section 5.4.

Table 5.4. Characterization and electrocatalytic properties of N-GNP: nitrogen content and distribution of nitrogen configurations (determined by XPS), BET surface area and number of transferred electrons for ORR estimated from RDE measurements.

Sample [a]	Surface N (at.%)	N pyridinic (at.%)	N graphtic (at.%)	N oxide (at.%)	BET surface area (m²/g)	Transferred electrons [b]
N-GNP1	1.9	0.66	0.96	0.28	552	3.3
N-GNP2	3.3	1.26	1.59	0.41	405	2.9
N-GNP3	1.6	0.61	0.78	0.21	537	3.5

[a] Abbreviations: N-GNP obtained from f-GNP with: BMIBF$_4$ (N-GNP1), PVI (N-GNP2) and PBVIBr (N-GNP3). [b] Average in the potential range from -0.3V to -0.5V

5.7 ORR activity of N-GNPs

CVs recorded in deaerated electrolyte (Figure 5.14 a) clearly show lower capacitive currents for N-GNPs compared to the pristine GNP. BET surface area measurements (Table 5.4) corroborate the lower electroactive surface area with values in the range of 405-552 m^2/g for N-GNP samples, in contrast with 622 m^2/g for the pristine GNP. Hence, N-doping leads to 11-35% decrease in the surface area with the most pronounced effect on N-GNP2 (doped by the neutral polymer PVI). In addition, a denser and more compact morphology was observed in SEM images for N-GNPs (in Pub.V), with a clear loss of porosity compared to pristine GNP.

CVs in O_2-saturated electrolyte (figure 5.14b) reveal the enhancement in ORR electrocatalytic activity for N-GNP samples compared with pristine GNPs. Figure 5.14c shows the number of transferred electrons for the samples, obtained by RDE measurements and the corresponding K-L plots (Figure 5 in Pub.V). It can be seen that the ORR electrocatalytic activity is considerably improved in N-GNPs especially with N-GNP1 and N-GNP3, doped using IL and PIL precursors, respectively. The average electron number in the range of -0.3 to -0.5 V were 3.5, 3.3 and 2.9, respectively for N-GNP3, N-GNP1 and N-GNP2.
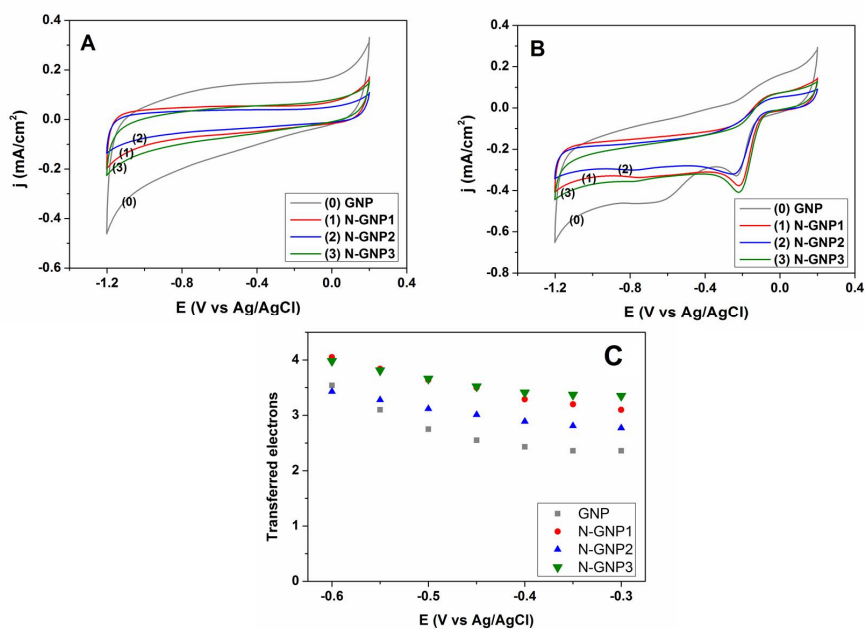
Figure 5.14. CVs of N-GNPs in A) N2-saturated and B) O2-sat. 0.1 M KOH. C) Number of transferred electrons for ORR vs. potential for N-GNPs compared to pristine GNP.

In these samples ORR activity cannot be related to the total nitrogen loadings, since N-GNP3 and N-GNP1with higher ORR electrocatalytic activity contain less nitrogen atoms (Table 5.4). These results are in agreement with numerous studies claiming that the activity does not necessarily correlate with total N content [18, 133]. On the other hand, better ORR activity of N-GNP3 and N-

GNP1 cannot be explained by the dominance of graphitic-N type, since the three N-GNP samples contain very similar relative proportion of N-functionalities. However, N-GNP3 and N-GNP1 exhibited larger BET surface area (537-552 m^2/g) than N-GNP1 (405 m^2/g), suggesting that the electrocatalytic activity is more influenced by the BET surface area of the N-GNPs. These results are in agreement with previous studies suggesting that the microporous surface area and accessibility to active sites was the main factor affecting the ORR catalytic activity in Fe/N/C catalysts produced from carbon black [152]. Similarly, the excellent catalytic activity of our N-FWCNT with low nitrogen content was caused by highly accessible N-sites.

From the results, it can be postulated that the ionic nature of IL and PIL used in this study not only influences the enhanced interaction of the precursor with the GNP sheets, but also that the anions in these compounds (BF_4^- in $BMIBF_4$ and Br^- in PBVIBr) seem to act as a porogen during pyrolysis of the functionalized GNPs. Such a promising effect on porosity was not observed using natural polymer PVI, which leads to a very pronounced decrease in surface area (35%) with respect to pristine GNP. Therefore, active surface area and consequently accessibility to catalytic sites can facilitate the ORR activity. The wrinkles and disordered structure of graphene sheets along with the increased surface area could facilitate the adsorption of O_2, which would be advantageous for ORR activity [133].

6 Conclusions

The thesis presented the significant influence of different carbon nanomaterials (CNMs) on the fuel cell electrodes and their overall performance. Catalysts for methanol oxidation and oxygen reduction reaction were synthesized based on CNMs, with special emphasis on assessing their performance in the actual fuel cell environment in order to maximize their electrocatalytic activity and stability compared to current commercial catalysts. CNMs were used for different roles, acting both as support for PtRu catalysts to catalyze the MOR and as Pt-free electrocatalysts for the ORR in alkaline media. The research work also provided further knowledge for the suitable selection of CNMs, the influence of the catalyst layer structure and fuel cell components on the overall performance and stability of certain catalyst materials. The major conclusions of the dissertation can be summarized as follows:

PtRu-catalysts were deposited on three different nanocarbon supports: carbon black, FWCNTs and GNFs. A special care to control the synthesis method enabled us to produce catalysts of comparable size and composition on the different supports using a polyol method. It was possible to evaluate the influence of the carbon supports at the anode by neglecting differences arising from the catalyst size. Both electrochemical characterization of catalyst films and 6-day long stability measurements in methanol fuel cells were done. It was found that GNF-supported electrocatalyst presented the most stable performance during 6 days, which illustrated the potential application of this novel nanocarbon as a more stable fuel cell component (Pub.1).

As it is very important to develop miniaturized systems for portable power sources based on DMFC, the performance of the catalyst materials was also evaluated in a Si-micro fabricated DMFC. A special Si-nanograss structure was used as alternative for a traditional diffusion layer to simplify the assembly of the cell. The long-term performance (3-days) of PtRu-catalysts supported on Vulcan, FWCNTs and GNFs was evaluated in this micro-fuel cell. FWCNTs showed the best performance followed by GNFs, and both showed superior activity than the Vulcan supported catalyst. However, the fuel cell performance of the three materials did not follow the same trend as in macro-fuel cell (Pub.1). It was concluded that, when using different fuel cell systems to assess the performance of specific catalysts, the measurements should be carefully controlled to mimic each other as much as possible because even small changes in fuel cell components or conditions can lead to very different results. Moreover, we suggested that the Si-microfabricated DMFC can be a fast and cheap tool for catalyst material screening, due to the faster fabrication, assembly and lower amount of catalyst needed for testing (Pub.2).

Performance and stability of the methanol fuel cell with PtRu-GNFs electrocatalyst was improved by optimizing the anode layer structure. This was done by optimizing the Nafion content (ionomer to carbon ratio) of the electrode in membrane electrode assemblies. It was found that electrode containing 50 wt.% Nafion was the most stable during the long-term (9-days) fuel cell tests. This study revealed the importance of the electrode structure (in addition to the catalyst and support

effects). This optimization leads to a better ionomer-electrocatalyst interaction, lower electrical resistance and a suitable distribution of secondary pores for penetration of reactants and products that result in low mass transfer resistance along the electrode network (Pub.3).

Pt-free electrocatalysts were synthesized by modifying FWCNT walls with nitrogen atoms via a post-treatment method using PANI. The resulting N-FWCNTs showed high electrocatalytic activity for ORR in alkaline media. Despite a significantly lower nitrogen content (~0.5 at.%) compared to the literature, N-FWCNTs showed a high activity for ORR and performed on par with or better than a commercial Pt-C at the cathode of an alkaline DMFC. It can be concluded that the high activity of N-FWCNTs resulted from an efficient incorporation of N atoms in the open porous structure of the N-doped layer around the FWCNT wall in which the active sites are fully exposed for oxygen molecules. Simultaneously, the highly conductive FWCNT inner core was preserved for the electron conduction (Pub.4). We further suggested a *psudo-4e⁻* model for the ORR mechanism on N-FWCNTs in alkaline media, where oxygen molecules first electrochemically reduced to hydroperoxide on graphitic-N sites. Then, the generated hydroperoxde in the porous electrode moves on pyridinic-N sites and further electrochemically is reduced (to OH⁻) or chemically is decompose to oxygen.

Further studies on the electrocatalytic activity of N-GNPs were implemented. N-GNPs were synthesized by a facile post-treatment method using different imidazole-based derivatives, including a neutral polymer, an ionic liquid and a poly (ionic liquid). It was found that the final nitrogen content was correlated to the amount of nitrogen in the precursor. However, the ORR activity did not correlate with the nitrogen content or distribution of N-functionalities, rather it was determined by the porosity and accessibility of oxygen to the active sites in each type of N-GNP. Thus, the most active samples for ORR were N-GNPs synthesized by ionic liquids precursors (IL and PIL) which led to a more porous materials. These results can be inspiring in the choice of suitable precursors for doping CNMs with enhanced electrocatalytic activity for ORR (Pub.5).

In conclusion, DMFCs are considered as a promising power source for portable electronics, however they are yet facing a lot of challenges on their way to commercialization. There is still plenty of room to develop cost-efective electrocatalysts to achieve fully Pt-free DMFCs. As mentioned before, the alkaline system holds more promise for the use of Pt-free electrocatalysts. Therefore, further research should be implemented to develop alternative Pt-free anode catalysts for MOR. Recently, transition metal oxides (such as NiO) have received attention due to their low cost and facile synthesis [153, 154]. However, more research needs to be done in order to achieve more active and durable electrocatalysts than PtRu by modifying their synthesis methods and structures.

Regarding the use of N-doped CNMs as Pt-free electrocatalysts for the ORR, the exact role of the different N-functionalities on the ORR needs to be better understood. Further characterization is yet required to corroborate the proposed mechanism, which could be a topic for future research. In addition, improving the stability of N-FWCNTs would also be further improved.

7 References

[1] G. Merle, M. Wessling, K. Nijmeijer, Journal of Membrane Science 377 (2011) 1-35.
[2] O.Z. Sharaf, M.F. Orhan, Renewable and Sustainable Energy Reviews 32 (2014) 810-853.
[3] J.M. Sieben, M.M.E. Duarte, International Journal of Hydrogen Energy 37 (2012) 9941-9947.
[4] DOE-EERE, http://energy.gov/eere/fuelcells/fuel-cell-technology-challenges.
[5] J.N. Tiwari, R.N. Tiwari, G. Singh, K.S. Kim, Nano Energy 2 (2013) 553-578.
[6] K. Matsumoto, T. Fujigaya, H. Yanagi, N. Nakashima, Advanced Functional Materials 21 (2011) 1089-1094.
[7] A. Aiyejina, M.K.S. Sastry, Journal of Fuel Cell Science and Technology 9 (2011) 011011-011011.
[8] S. Park, J.-W. Lee, B.N. Popov, International Journal of Hydrogen Energy 37 (2012) 5850-5865.
[9] C. Heitner-Wirguin, Journal of Membrane Science 120 (1996) 1-33.
[10] B. Bauer, H. Strathmann, F. Effenberger, Desalination 79 (1990) 125-144.
[11] Y. Wang, K.S. Chen, J. Mishler, S.C. Cho, X.C. Adroher, Applied Energy 88 (2011) 981-1007.
[12] L. Yang, Y. Zhao, S. Chen, Q. Wu, X. Wang, Z. Hu, Chinese Journal of Catalysis 34 (2013) 1986-1991.
[13] E. Antolini, Applied Catalysis B: Environmental 88 (2009) 1-24.
[14] H. Liu, C. Song, L. Zhang, J. Zhang, H. Wang, D.P. Wilkinson, Journal of Power Sources 155 (2006) 95-110.
[15] P. Trogadas, T.F. Fuller, P. Strasser, Carbon 75 (2014) 5-42.
[16] S. Sharma, B.G. Pollet, Journal of Power Sources 208 (2012) 96-119.
[17] http://www.britannica.com/EBchecked/topic/221916/fullerene.
[18] H. Wang, T. Maiyalagan, X. Wang, ACS Catalysis 2 (2012) 781-794.
[19] M.J. Allen, V.C. Tung, R.B. Kaner, Chemical Reviews 110 (2009) 132-145.
[20] D. He, K. Cheng, H. Li, T. Peng, F. Xu, S. Mu, M. Pan, Langmuir 28 (2012) 3979-3986.
[21] H.-J. Choi, S.-M. Jung, J.-M. Seo, D.W. Chang, L. Dai, J.-B. Baek, Nano Energy 1 (2012) 534-551.
[22] P. Serp, M. Corrias, P. Kalck, Applied Catalysis A: General 253 (2003) 337-358.
[23] J.-S. Zheng, X.-S. Zhang, P. Li, J. Zhu, X.-G. Zhou, W.-K. Yuan, Electrochemistry Communications 9 (2007) 895-900.
[24] B. Kuppan, P. Selvam, Progress in Natural Science: Materials International 22 (2012) 616-623.
[25] Y. Liu, M. Wei, J. Qu, L. Mao, Journal of the Chinese Chemical Society 61 (2014) 404-408.
[26] T. Yoshitake, Y. Shimakawa, S. Kuroshima, H. Kimura, T. Ichihashi, Y. Kubo, D. Kasuya, K. Takahashi, F. Kokai, M. Yudasaka, S. Iijima, Physica B: Condensed Matter 323 (2002) 124-126.
[27] K.-W. Park, Y.-E. Sung, S. Han, Y. Yun, T. Hyeon, The Journal of Physical Chemistry B 108 (2003) 939-944.
[28] V.S. Bagotzky, Y.B. Vassilyev, Electrochimica Acta 12 (1967) 1323-1343.
[29] T. Iwasita, Electrochimica Acta 47 (2002) 3663-3674.
[30] V.S. Bagotzky, Y.B. Vassiliev, O.A. Khazova, Journal of Electroanalytical Chemistry and Interfacial Electrochemistry 81 (1977) 229-238.
[31] H. Wang, H. Baltruschat, The Journal of Physical Chemistry C 111 (2007) 7038-7048.
[32] H. Wang, T. Löffler, H. Baltruschat, Journal of Applied Electrochemistry 31 (2001) 759-765.

[33]   A.V. Tripković, K.D. Popović, B.N. Grgur, B. Blizanac, P.N. Ross, N.M. Marković, Electrochimica Acta 47 (2002) 3707-3714.
[34]   A.V. Tripković, K.D. Popović, J.D. Lović, V.M. Jovanović, A. Kowal, Journal of Electroanalytical Chemistry 572 (2004) 119-128.
[35]   J. Wu, X.Z. Yuan, J.J. Martin, H. Wang, J. Zhang, J. Shen, S. Wu, W. Merida, Journal of Power Sources 184 (2008) 104-119.
[36]   C. Song, J. Zhang, in: J. Zhang (Ed.), PEM Fuel Cell Electrocatalysts and Catalyst Layers, Springer London, 2008, pp. 89-134.
[37]   I. Kruusenberg, L. Matisen, H. Jiang, M. Huuppola, K. Kontturi, K. Tammeveski, Electrochemistry Communications 12 (2010) 920-923.
[38]   K. Vaik, A. Sarapuu, K. Tammeveski, F. Mirkhalaf, D.J. Schiffrin, Journal of Electroanalytical Chemistry 564 (2004) 159-166.
[39]   N.M. Marković, P.N. Ross Jr, Surface Science Reports 45 (2002) 117-229.
[40]   E. G. Rakov, D. A.Grishin, Yu. V. Gavrilov, E. V.Rakova, A. G. Nasibulin, H. Jiang, E.I. Kauppinen, Russian J of Phys. Chem. 78 (2004) 1966.
[41]   A. J. Bard, L.R. Faulkner, Wiley 2nd ed. (2001).
[42]   StrmcnikD, KodamaK, D. van der Vliet, GreeleyJ, V.R. Stamenkovic, N.M. Marković, Nat Chem 1 (2009) 466-472.
[43]   J. Nikolic, E. Expósito, J. Iniesta, J. González-Garcia, V. Montiel, Journal of Chemical Education 77 (2000) 1191.
[44]   http://www.lanl.gov/orgs/mpa/mpa11/breakthrough1.htm.
[45]   P. Kanninen, Doctoral dissertation 76 (2014).
[46]   S.N. Stamatin, M. Borghei, S.M. Andersen, S. Veltze, V. Ruiz, E. Kauppinen, E.M. Skou, International Journal of Hydrogen Energy 39 (2014) 8215-8224.
[47]   M.R. Berber, I.H. Hafez, T. Fujigaya, N. Nakashima, Journal of Materials Chemistry A 2 (2014) 19053-19059.
[48]   X. Yu, S. Ye, Journal of Power Sources 172 (2007) 145-154.
[49]   S.M. Andersen, M. Borghei, P. Lund, Y.-R. Elina, A. Pasanen, E. Kauppinen, V. Ruiz, P. Kauranen, E.M. Skou, Solid State Ionics 231 (2013) 94-101.
[50]   D. Sebastián, I. Suelves, E. Pastor, R. Moliner, M.J. Lázaro, Applied Catalysis B: Environmental 132–133 (2013) 13-21.
[51]   S.-M. Park, D.-H. Jung, S.-K. Kim, S. Lim, D. Peck, W.H. Hong, Electrochimica Acta 54 (2009) 3066-3072.
[52]   Y. Feng, H. Zhang, Y. Hou, T.P. McNicholas, D. Yuan, S. Yang, L. Ding, W. Feng, J. Liu, ACS Nano 2 (2008) 1634-1638.
[53]   S. Kundu, Y. Wang, W. Xia, M. Muhler, The Journal of Physical Chemistry C 112 (2008) 16869-16878.
[54]   E. Yli-Rantala, A. Pasanen, P. Kauranen, V. Ruiz, M. Borghei, E. Kauppinen, A. Oyarce, G. Lindbergh, C. Lagergren, M. Darab, S. Sunde, M. Thomassen, S. Ma-Andersen, E. Skou, Fuel Cells 11 (2011) 715-725.
[55]   C. Jin, T.C. Nagaiah, W. Xia, B. Spliethoff, S. Wang, M. Bron, W. Schuhmann, M. Muhler, Nanoscale 2 (2010) 981-987.
[56]   W. Xia, C. Jin, S. Kundu, M. Muhler, Carbon 47 (2009) 919-922.
[57]   A.S. Aricò, S. Srinivasan, V. Antonucci, Fuel Cells 1 (2001) 133-161.
[58]   H. Bönnemann, U. Endruschat, J. Hormes, G. Köhl, S. Kruse, H. Modrow, R. Mörtel, K.S. Nagabhushana, Fuel Cells 4 (2004) 297-308.
[59]   M.C. Denis, M. Lefèvre, D. Guay, J.P. Dodelet, Electrochimica Acta 53 (2008) 5142-5154.
[60]   X. Xue, C. Liu, W. Xing, T. Lu, Journal of The Electrochemical Society 153 (2006) E79-E84.
[61]   P. Sivakumar, V. Tricoli, Electrochemical and Solid-State Letters 9 (2006) A167-A170.
[62]   A. Caillard, C. Coutanceau, P. Brault, J. Mathias, J.M. Léger, Journal of Power Sources 162 (2006) 66-73.
[63]   Z. He, J. Chen, D. Liu, H. Zhou, Y. Kuang, Diamond and Related Materials 13 (2004) 1764-1770.
[64]   S. Eriksson, U. Nylén, S. Rojas, M. Boutonnet, Applied Catalysis A: General 265 (2004) 207-219.

[65]   S. Rojas, F.J. García-García, S. Järas, M.V. Martínez-Huerta, J.L.G. Fierro, M. Boutonnet, Applied Catalysis A: General 285 (2005) 24-35.
[66]   S.B. Yoon, B. Fang, M. Kim, J.H. Kim, J.-S. Yu, in: W. Gerhard (Ed.), Frontiers of Nanoscience, Elsevier, 2009, pp. 173-231.
[67]   H. Bönnemann, R. Brinkmann, S. Kinge, T.O. Ely, M. Armand, Fuel Cells 4 (2004) 289-296.
[68]   A. Esmaeilifar, S. Rowshanzamir, M.H. Eikani, E. Ghazanfari, Energy 35 (2010) 3941-3957.
[69]   H.-S. Oh, J.-G. Oh, Y.-G. Hong, H. Kim, Electrochimica Acta 52 (2007) 7278-7285.
[70]   M. Tsuji, M. Kubokawa, R. Yano, N. Miyamae, T. Tsuji, M.-S. Jun, S. Hong, S. Lim, S.-H. Yoon, I. Mochida, Langmuir 23 (2007) 387-390.
[71]   T.K. Lee, H.J. Park, M.K. Kwon, J.H. Jung, J. Kim, S.H. Hur, Journal of Nanomaterials 2012 (2012) 6.
[72]   C.-C. Chien, K.-T. Jeng, Materials Chemistry and Physics 99 (2006) 80-87.
[73]   L. Li, Y. Xing, The Journal of Physical Chemistry C 111 (2007) 2803-2808.
[74]   Y. Ma, S. Jiang, G. Jian, H. Tao, L. Yu, X. Wang, X. Wang, J. Zhu, Z. Hu, Y. Chen, Energy & Environmental Science 2 (2009) 224-229.
[75]   C.A. Bessel, K. Laubernds, N.M. Rodriguez, R.T.K. Baker, The Journal of Physical Chemistry B 105 (2001) 1115-1118.
[76]   W.F. Lin, T. Iwasita, W. Vielstich, The Journal of Physical Chemistry B 103 (1999) 3250-3257.
[77]   Y. Lin, X. Cui, C.H. Yen, C.M. Wai, Langmuir 21 (2005) 11474-11479.
[78]   M. Uchida, Y. Aoyama, N. Eda, A. Ohta, Journal of The Electrochemical Society 142 (1995) 4143-4149.
[79]   X. Wang, W. Li, Z. Chen, M. Waje, Y. Yan, Journal of Power Sources 158 (2006) 154-159.
[80]   P.J. Ferreira, G.J. la O', Y. Shao-Horn, D. Morgan, R. Makharia, S. Kocha, H.A. Gasteiger, Journal of The Electrochemical Society 152 (2005) A2256-A2271.
[81]   S. Ma, Q. Chen, F.H. Jøgensen, P.C. Stein, E.M. Skou, Solid State Ionics 178 (2007) 1568-1575.
[82]   C. Wannek, S. Nehr, M. Vahlenkamp, J. Mergel, D. Stolten, Journal of Applied Electrochemistry 40 (2010) 29-38.
[83]   M.A. Abdelkareem, T. Tsujiguchi, N. Nakagawa, Journal of Power Sources 195 (2010) 6287-6293.
[84]   B. Krishnamurthy, S. Deepalochani, K.S. Dhathathreyan, Fuel Cells 8 (2008) 404-409.
[85]   R. Jasinski, Nature 201 (1964) 1212-1213.
[86]   J. Pavez, M. Páez, A. Ringuedé, F. Bedioui, J. Zagal, J Solid State Electrochem 9 (2005) 21-29.
[87]   J. Zagal, M. Páez, A.A. Tanaka, J.R. dos Santos Jr, C.A. Linkous, Journal of Electroanalytical Chemistry 339 (1992) 13-30.
[88]   J.-P. Dodelet, in: J. Zagal, F. Bedioui, J.-P. Dodelet (Eds.), N4-Macrocyclic Metal Complexes, Springer New York, 2006, pp. 83-147.
[89]   C.W.B. Bezerra, L. Zhang, K. Lee, H. Liu, A.L.B. Marques, E.P. Marques, H. Wang, J. Zhang, Electrochimica Acta 53 (2008) 4937-4951.
[90]   S. Gupta, D. Tryk, I. Bae, W. Aldred, E. Yeager, Journal of Applied Electrochemistry 19 (1989) 19-27.
[91]   G. Liu, X. Li, P. Ganesan, B.N. Popov, Electrochimica Acta 55 (2010) 2853-2858.
[92]   D. Ohms, S. Herzog, R. Franke, V. Neumann, K. Wiesener, S. Gamburcev, A. Kaisheva, I. Iliev, Journal of Power Sources 38 (1992) 327-334.
[93]   H. Wang, R. Côté, G. Faubert, D. Guay, J.P. Dodelet, The Journal of Physical Chemistry B 103 (1999) 2042-2049.
[94]   R. Có⁄té, G. Lalande, D. Guay, J.P. Dodelet, G. Dénès, Journal of The Electrochemical Society 145 (1998) 2411-2418.
[95]   V.V. Strelko, V.S. Kuts, P.A. Thrower, Carbon 38 (2000) 1499-1503.
[96]   D. Srivastava, T. Susi, M. Borghei, L. Kari, RSC Advances 4 (2014) 15225-15235.
[97]   K. Gong, F. Du, Z. Xia, M. Durstock, L. Dai, Science 323 (2009) 760-764.

[98]   T. Susi, A. Kaskela, Z. Zhu, P. Ayala, R. Arenal, Y. Tian, P. Laiho, J. Mali, A.G. Nasibulin, H. Jiang, G. Lanzani, O. Stephan, K. Laasonen, T. Pichler, A. Loiseau, E.I. Kauppinen, Chemistry of Materials 23 (2011) 2201-2208.
[99]   S. Kundu, T.C. Nagaiah, W. Xia, Y. Wang, S.V. Dommele, J.H. Bitter, M. Santa, G. Grundmeier, M. Bron, W. Schuhmann, M. Muhler, The Journal of Physical Chemistry C 113 (2009) 14302-14310.
[100]   Z. Chen, D. Higgins, Z. Chen, Electrochimica Acta 55 (2010) 4799-4804.
[101]   T. Sharifi, F. Nitze, H.R. Barzegar, C.-W. Tai, M. Mazurkiewicz, A. Malolepszy, L. Stobinski, T. Wågberg, Carbon 50 (2012) 3535-3541.
[102]   D. Geng, H. Liu, Y. Chen, R. Li, X. Sun, S. Ye, S. Knights, Journal of Power Sources 196 (2011) 1795-1801.
[103]   J. Yin, Y. Qiu, J. Yu, Chemistry Letters 42 (2013) 413-415.
[104]   H.-S. Oh, J.-G. Oh, B. Roh, I. Hwang, H. Kim, Electrochemistry Communications 13 (2011) 879-881.
[105]   M. Vikkisk, I. Kruusenberg, U. Joost, E. Shulga, I. Kink, K. Tammeveski, Applied Catalysis B: Environmental 147 (2014) 369-376.
[106]   D. Long, W. Li, L. Ling, J. Miyawaki, I. Mochida, S.-H. Yoon, Langmuir 26 (2010) 16096-16102.
[107]   R. Liu, D. Wu, X. Feng, K. Müllen, Angewandte Chemie International Edition 49 (2010) 2565-2569.
[108]   S. Chen, J. Bi, Y. Zhao, L. Yang, C. Zhang, Y. Ma, Q. Wu, X. Wang, Z. Hu, Advanced Materials 24 (2012) 5593-5597.
[109]   G. Ma, R. Jia, J. Zhao, Z. Wang, C. Song, S. Jia, Z. Zhu, The Journal of Physical Chemistry C 115 (2011) 25148-25154.
[110]   C.V. Rao, C.R. Cabrera, Y. Ishikawa, The Journal of Physical Chemistry Letters 1 (2010) 2622-2627.
[111]   J.D. Wiggins-Camacho, K.J. Stevenson, The Journal of Physical Chemistry C 115 (2011) 20002-20010.
[112]   M. Glerup, J. Steinmetz, D. Samaille, O. Stéphan, S. Enouz, A. Loiseau, S. Roth, P. Bernier, Chemical Physics Letters 387 (2004) 193-197.
[113]   Z. Wang, R. Jia, J. Zheng, J. Zhao, L. Li, J. Song, Z. Zhu, ACS Nano 5 (2011) 1677-1684.
[114]   M. Reyes-Reyes, N. Grobert, R. Kamalakaran, T. Seeger, D. Golberg, M. Rühle, Y. Bando, H. Terrones, M. Terrones, Chemical Physics Letters 396 (2004) 167-173.
[115]   T.C. Nagaiah, S. Kundu, M. Bron, M. Muhler, W. Schuhmann, Electrochemistry Communications 12 (2010) 338-341.
[116]   M. Vikkisk, I. Kruusenberg, U. Joost, E. Shulga, K. Tammeveski, Electrochimica Acta 87 (2013) 709-716.
[117]   S. Ratso, I. Kruusenberg, M. Vikkisk, U. Joost, E. Shulga, I. Kink, T. Kallio, K. Tammeveski, Carbon 73 (2014) 361-370.
[118]   A.U. Haq, J. Lim, J.M. Yun, W.J. Lee, T.H. Han, S.O. Kim, Small 9 (2013) 3829-3833.
[119]   H. Zhong, H. Zhang, Z. Xu, Y. Tang, J. Mao, ChemSusChem 5 (2012) 1698-1702.
[120]   G. Wu, K.L. More, C.M. Johnston, P. Zelenay, Science 332 (2011) 443-447.
[121]   N. Ferrer-Anglada, M. Kaempgen, V. Skákalová, U. Dettlaf-Weglikowska, S. Roth, Diamond and Related Materials 13 (2004) 256-260.
[122]   E.N. Konyushenko, J. Stejskal, M. Trchová, J. Hradil, J. Kovářová, J. Prokeš, M. Cieslar, J.-Y. Hwang, K.-H. Chen, I. Sapurina, Polymer 47 (2006) 5715-5723.
[123]   L. Li, Z.-Y. Qin, X. Liang, Q.-Q. Fan, Y.-Q. Lu, W.-H. Wu, M.-F. Zhu, The Journal of Physical Chemistry C 113 (2009) 5502-5507.
[124]   K. Stańczyk, R. Dziembaj, Z. Piwowarska, S. Witkowski, Carbon 33 (1995) 1383-1392.
[125]   R. Arrigo, M. Havecker, R. Schlogl, D.S. Su, Chemical Communications (2008) 4891-4893.
[126]   T. Sharifi, G. Hu, X. Jia, T. Wågberg, ACS Nano 6 (2012) 8904-8912.
[127]   K. Chizari, A. Deneuve, O. Ersen, I. Florea, Y. Liu, D. Edouard, I. Janowska, D. Begin, C. Pham-Huu, ChemSusChem 5 (2012) 102-108.
[128]   D. Yu, E. Nagelli, F. Du, L. Dai, The Journal of Physical Chemistry Letters 1 (2010) 2165-2173.

[129]   G.-L. Tian, Q. Zhang, B. Zhang, Y.-G. Jin, J.-Q. Huang, D.S. Su, F. Wei, Advanced Functional Materials (2014) n/a-n/a.
[130]   J.M. Goran, J.L. Lyon, K.J. Stevenson, Analytical Chemistry 83 (2011) 8123-8129.
[131]   Z. Chen, D. Higgins, Z. Chen, Carbon 48 (2010) 3057-3065.
[132]   H.-S. Oh, J.-G. Oh, W.H. Lee, H.-J. Kim, H. Kim, International Journal of Hydrogen Energy 36 (2011) 8181-8186.
[133]   L. Lai, J.R. Potts, D. Zhan, L. Wang, C.K. Poh, C. Tang, H. Gong, Z. Shen, J. Lin, R.S. Ruoff, Energy & Environmental Science 5 (2012) 7936-7942.
[134]   S. Yasuda, L. Yu, J. Kim, K. Murakoshi, Chemical Communications 49 (2013) 9627-9629.
[135]   A. Bonakdarpour, M. Lefevre, R. Yang, F. Jaouen, T. Dahn, J.-P. Dodelet, J.R. Dahn, Electrochemical and Solid-State Letters 11 (2008) B105-B108.
[136]   F. Jaouen, The Journal of Physical Chemistry C 113 (2009) 15433-15443.
[137]   F.d.r. Jaouen, J.-P. Dodelet, The Journal of Physical Chemistry C 113 (2009) 15422-15432.
[138]   P. Kanninen, M. Borghei, O. Sorsa, E. Pohjalainen, E.I. Kauppinen, V. Ruiz, T. Kallio, Applied Catalysis B: Environmental 156–157 (2014) 341-349.
[139]   F. Schedin, A.K. Geim, S.V. Morozov, E.W. Hill, P. Blake, M.I. Katsnelson, K.S. Novoselov, Nat Mater 6 (2007) 652-655.
[140]   G. Giovannetti, P.A. Khomyakov, G. Brocks, V.M. Karpan, J. van den Brink, P.J. Kelly, Physical Review Letters 101 (2008) 026803.
[141]   W. Chen, S. Chen, D.C. Qi, X.Y. Gao, A.T.S. Wee, Journal of the American Chemical Society 129 (2007) 10418-10422.
[142]   L.S. Panchakarla, K.S. Subrahmanyam, S.K. Saha, A. Govindaraj, H.R. Krishnamurthy, U.V. Waghmare, C.N.R. Rao, Advanced Materials 21 (2009) 4726-4730.
[143]   D. Wei, Y. Liu, Y. Wang, H. Zhang, L. Huang, G. Yu, Nano Letters 9 (2009) 1752-1758.
[144]   C. Zhang, L. Fu, N. Liu, M. Liu, Y. Wang, Z. Liu, Advanced Materials 23 (2011) 1020-1024.
[145]   D. Deng, X. Pan, L. Yu, Y. Cui, Y. Jiang, J. Qi, W.-X. Li, Q. Fu, X. Ma, Q. Xue, G. Sun, X. Bao, Chemistry of Materials 23 (2011) 1188-1193.
[146]   R. Imran Jafri, N. Rajalakshmi, S. Ramaprabhu, Journal of Materials Chemistry 20 (2010) 7114-7117.
[147]   Y. Shao, S. Zhang, M.H. Engelhard, G. Li, G. Shao, Y. Wang, J. Liu, I.A. Aksay, Y. Lin, Journal of Materials Chemistry 20 (2010) 7491-7496.
[148]   N.G. Shang, P. Papakonstantinou, S. Sharma, G. Lubarsky, M. Li, D.W. McNeill, A.J. Quinn, W. Zhou, R. Blackley, Chemical Communications 48 (2012) 1877-1879.
[149]   J. Lu, J.-x. Yang, J. Wang, A. Lim, S. Wang, K.P. Loh, ACS Nano 3 (2009) 2367-2375.
[150]   X. Wang, P.F. Fulvio, G.A. Baker, G.M. Veith, R.R. Unocic, S.M. Mahurin, M. Chi, S. Dai, Chemical Communications 46 (2010) 4487-4489.
[151]   J.-Y. Liu, H.-Y. Chang, Q.D. Truong, Y.-C. Ling, Journal of Materials Chemistry C 1 (2013) 1713-1716.
[152]   F. Jaouen, M. Lefèvre, J.-P. Dodelet, M. Cai, The Journal of Physical Chemistry B 110 (2006) 5553-5558.
[153]   C.D. Gu, M.L. Huang, X. Ge, H. Zheng, X.L. Wang, J.P. Tu, International Journal of Hydrogen Energy 39 (2014) 10892-10901.
[154]   D. Yu, X. Zhang, K. Wang, L. He, J. Yao, Y. Feng, H. Wang, International Journal of Hydrogen Energy 38 (2013) 11863-11869.

Direct methanol fuel cells (DMFC) are great candidates for portable power source applications due to the high energy density of methanol, easy storage and recharging. The sluggish kinetics of the methanol oxidation reaction at the anode and oxygen reduction reaction (ORR) at the cathode are key challenges in DMFC technology. The state-of-the-art catalysts are Pt-based catalysts supported on Carbon black. However, the high price of Pt, corrosion of carbon support and Pt aggregation which result in fuel cell instability are the main problems.

In this thesis, Pt nanoparticles deposited on different types of carbon nanomaterials were used at the anode electrode in order to improve the stability of DMFC. In addition, highly active electrocatalysts for ORR were synthesized by nitrogen doping of carbon nanomaterial, which showed similar performace to commercial Pt-C at the cathode side of DMFC.

BUSINESS +
ECONOMY

ART +
DESIGN +
ARCHITECTURE

SCIENCE +
TECHNOLOGY

CROSSOVER

DOCTORAL
DISSERTATIONS